

# POLITECNICO DI TORINO

Master's Degree in Aerospace engineering



Master's Degree Thesis

## Design and Modeling of an Autonomous Parafoil for Rover Mars Landing

Supervisors

Prof. Elisa CAPELLO

Dr. Mauro MANCINI

Candidate

Alessandro MERCURIO

April 2021

## Abstract

There are many ways to study space objects, such as using telescopes on Earth, satellites and orbiters near the study object or rovers on its surface. Some planets and moons of our Solar system have an atmosphere, and in the last decades new types of vehicles, like drones, conventional airplanes or lighter-than-atmosphere vehicles, were designed to explore these space objects in a new way.

These types of vehicles, called aerobots, enable to have a greater range of exploration than rovers, and also a higher resolution of images and information than an orbiter, but for obvious reasons can be applied only in planets or moons with an atmosphere, like Mars, Venus and Titan.

In this thesis two different types of aerobots are presented for a mission on Mars: a drone and a parafoil, which have very different characteristics and applications. The first one can be used to explore unreachable regions for a conventional rover, like caves or deep craters, and to identify appropriate future human landing sites. On the other hand the parafoil system can be used for autonomous precise landings: it is a good compromise between a conventional airplane, which is more controllable, and a parachute or a balloon, which are lighter and easier to transport inside a space vehicle.

Even if both aerobots are considered, this thesis is focusing on the modeling and design of the parafoil system. For this reason in the first part an introduction to space drones and aerobots for space exploration is presented. Moreover, drone and parafoil dynamics and kinematics and mars environment model are also included. In the second part the design and modeling of the parafoil's dynamics simulator is discussed for studying the feasibility of the system and its behavior in the martian atmosphere.

The thesis outlines the preliminary design of the parafoil to fly in the thin martian atmosphere. Then a 6 DoF (Degrees of Freedom) trajectory simulator is developed, without taking into account the apparent mass effect, due to the low density of the martian atmosphere. A lateral track proportional control law has been selected as guidance algorithm, which generates the reference command for the actuators using inertial velocities and position of the parafoil. This guidance algorithm was also tested with the implementation of a wind model to study the performance of the system.

# Acknowledgements

*I would like to thank supervisors Prof. Elisa Capello and Dr. Mauro Mancini who guided me and supported me through this work and made me discover the potential of aerobots in space exploration. I want also to thank Giovanni Piccione, my thesis colleague, who shared all this journey with me.*

*Moreover i would like to thank my family, my girlfriend and my friends for supporting me for all these years.*



# Table of Contents

<b>List of Tables</b>	v
<b>List of Figures</b>	vi
<b>Acronyms</b>	x
<b>1 Introduction</b>	1
1.1 Research objectives . . . . .	1
1.2 Possible target planets . . . . .	3
1.2.1 Venus . . . . .	3
1.2.2 Titan . . . . .	4
1.2.3 Mars . . . . .	5
1.3 Mars aerobots background . . . . .	7
1.3.1 Fixed-wing . . . . .	7
1.3.2 Rotary-wings . . . . .	8
1.3.3 LTA vehicles . . . . .	11
1.3.4 Flapping-wings . . . . .	12
<b>2 Mathematical models</b>	13
2.1 Mars environment . . . . .	13
2.2 Reference frame . . . . .	16
2.2.1 Mars Inertial Frame . . . . .	16
2.2.2 Body Frame . . . . .	16
2.3 Gravity model . . . . .	18
2.4 Atmosphere model . . . . .	19
2.5 Wind model . . . . .	19
2.6 Drone's models . . . . .	22
2.6.1 Kinematics model . . . . .	24
2.6.2 Dynamics model . . . . .	25
2.7 Parafoil's models . . . . .	26
2.7.1 Kinematics model . . . . .	27

2.7.2	Dynamics model . . . . .	28
<b>3</b>	<b>Parafoil’s dynamics simulator</b>	<b>34</b>
3.1	The rover . . . . .	36
3.2	Parafoil’s design . . . . .	36
3.2.1	Aerodynamic features . . . . .	38
3.2.2	Parafoil’s dimensions . . . . .	45
3.3	Simulator’s structure . . . . .	48
3.3.1	GNC . . . . .	50
<b>4</b>	<b>Tests and results</b>	<b>54</b>
4.1	Trajectory . . . . .	56
4.2	Performance with wind disturbances . . . . .	60
<b>5</b>	<b>Conclusion and future works</b>	<b>67</b>
5.1	Conclusion . . . . .	67
5.2	Future works . . . . .	68
<b>A</b>	<b>Drone’s dynamics simulator</b>	<b>70</b>
A.1	Drone configuration . . . . .	71
A.1.1	Iterative loop . . . . .	76
A.2	Guidance and Control . . . . .	78
A.2.1	Guidance algorithm . . . . .	78
A.2.2	Control design . . . . .	79
A.3	Actuators . . . . .	81
A.4	Test and Results . . . . .	81
A.4.1	Hoovering . . . . .	82
A.5	Square maneuver . . . . .	83
A.6	Conclusions . . . . .	85
	<b>Bibliography</b>	<b>87</b>

# List of Tables

1.1	comparison between Earth and Mars . . . . .	6
1.2	ARES-2 Mars drone parameters . . . . .	8
1.3	Merits and Limitations of Large and Small Mars Rotorcrafts . . . . .	9
1.4	Mars Ingenuity features . . . . .	10
2.1	Comparison of Relevant Earth and Mars Parameters . . . . .	14
2.2	apparent masses and inertias comparison between Earth and Mars for a parafoil of 13 m <sup>2</sup> wing surface . . . . .	33
3.1	Rover's characteristics . . . . .	36
3.2	Parafoil's parameters . . . . .	37
3.3	Longitudinal dynamics . . . . .	43
3.4	Lateral-Directional Derivatives . . . . .	44
3.5	Control Derivatives . . . . .	45
3.6	Parafoil's geometric features . . . . .	46
3.7	Total moment of inertia of the parafoil system . . . . .	48
3.8	controllers parameters . . . . .	53
A.1	Selected propeller's data . . . . .	73
A.2	DJI E305 peculiarity . . . . .	74
A.3	lithium polymer battery (Li-Po S4) peculiarity . . . . .	74
A.4	Drone configuration parameters . . . . .	78

# List of Figures

1.1	profile of Venus's atmosphere . . . . .	3
1.2	rotary wing decelerator for Venus probe by Young . . . . .	4
1.3	Solar Venus drone designed by Landis . . . . .	4
1.4	Titan's atmosphere profile . . . . .	5
1.5	Titan's drone concepts: Dragonfly and Montgolfiere baloon flagship	5
1.6	average Mars atmosphere parameters versus altitude . . . . .	6
1.7	ARES-2 configurations for Mars exploration . . . . .	8
1.8	Representation of Mars Helicopter Ingenuity on the surface of Mars	10
1.9	A schematic view of a flying wing with vertical and horizontal flight modes . . . . .	10
1.10	View of designed and manufactured Balloon Guidance System for Mars exploration . . . . .	11
1.11	Parafoil model . . . . .	12
1.12	View of Entomompter designed by Colozza for Mars exploration . .	12
2.1	Illustration of Martian Solar Longitude Diagram . . . . .	13
2.2	A Comparison of Rotor Thrust Generated on Earth and Mars . . .	15
2.3	Mars Inertial Reference System . . . . .	16
2.4	Body Reference Frame for drone and parafoil system . . . . .	17
2.5	Global Gravity Map of Mars . . . . .	18
2.6	Average wind in Mars during winter at 10m altitude . . . . .	20
2.7	Average wind with Bias of 10% . . . . .	21
2.8	Average wind with Bias of 10% and Noise . . . . .	21
2.9	Wind model operating diagram . . . . .	22
2.10	Example of Bicopter . . . . .	22
2.11	Example of Tricopter "Y" shaped . . . . .	23
2.12	Example of Quadcopter "+" and "x" shaped . . . . .	23
2.13	The ram-air parachute . . . . .	26
2.14	Free body configuration of the parafoil-payload system. . . . .	27
2.15	Volumetric Representation of Apparent Masses and Moments . . . .	33

3.1	Parafoil system simulator flow chart . . . . .	35
3.2	JPL's open source rover . . . . .	36
3.3	Definition of anhedral angle for a ram-air wing . . . . .	37
3.4	Theoretical section lift coefficient for an 18% Clark Y ram-air parachute airfoil . . . . .	38
3.5	Experimental and theoretical lift coefficients for a ram-air wing, $AR = 3.0$ . . . . .	39
3.6	$\delta$ for rectangular planform wings versus aspect ratio . . . . .	40
3.7	Experimental and theoretical drag coefficient for a ram-air wing, $AR = 3.0$ . . . . .	41
3.8	Definitions for static stability analysis . . . . .	42
3.9	Parafoil system Simulink model . . . . .	49
3.10	Examples of open-loop and closed-loop control systems . . . . .	50
3.11	Overall GNC architecture . . . . .	51
3.12	Position controller . . . . .	52
3.13	Attitude controller . . . . .	52
4.1	Parafoil's attitude . . . . .	54
4.2	Parafoil's velocities . . . . .	55
4.3	Parafoil's angular velocities . . . . .	55
4.4	Parafoil's position . . . . .	56
4.5	Parafoil's velocities . . . . .	56
4.6	Parafoil's attitude . . . . .	57
4.7	Parafoil's angular velocities . . . . .	57
4.8	Comparison between two types of trajectories . . . . .	58
4.9	Comparison between two types of trajectories: upper view . . . . .	58
4.10	Possible landing trajectories . . . . .	59
4.11	Possible landing trajectories: upper view . . . . .	59
4.12	Comparison between trajectory with and without wind . . . . .	60
4.13	Comparison between trajectory with and without wind: upper view . . . . .	61
4.14	Parafoil's attitude with and without wind disturbance . . . . .	61
4.15	Parafoil's angular velocities with and without wind disturbance . . . . .	62
4.16	Parafoil's velocities with and without wind disturbance . . . . .	62
4.17	Comparison between trajectory with and without wind . . . . .	63
4.18	Comparison between trajectory with and without wind: upper view . . . . .	63
4.19	Parafoil's attitude with and without wind disturbance in spiral descent . . . . .	64
4.20	Parafoil's angular velocities with and without wind disturbance in spiral descent . . . . .	64
4.21	Parafoil's velocities with and without wind disturbance in spiral descent . . . . .	65
4.22	Switch block flow chart . . . . .	65

4.23	Comparison between trajectory with and without wind, with new switch block . . . . .	66
4.24	Comparison between trajectory with and without wind, with new switch block: upper view . . . . .	66
A.1	Drone's simulator . . . . .	71
A.2	Values of $C_t$ and $C_q$ as the angular velocity varies . . . . .	72
A.3	mass as a function of radius for drone propellers and model helicopter propellers . . . . .	73
A.4	Drone's flowchart . . . . .	77
A.5	Guidance algorithm structure . . . . .	79
A.6	PID controller basical structure . . . . .	79
A.7	Cascade controller structure . . . . .	80
A.8	Error in caused by wind during Hovering maneuver . . . . .	82
A.9	Attitude angles during Hovering maneuver . . . . .	83
A.10	Trajectory of the drone in Square maneuver . . . . .	84
A.11	Output of Square pattern . . . . .	84



# Acronyms

**LTA**

Lighter-than-atmosphere

**UAV**

Unmanned aerial vehicle

**PADS**

Precise aerial delivery system

**DoF**

Degrees of freedom

**NASA**

National Aeronautics and Space Administration

**JPL**

Jet Propulsion Laboratory

**MAV**

Micro Air Vehicles

**NED**

North-East-Down Reference System

**MI**

Martian Inertial reference frame

**CoM**

Centre of Mass

**CCW**

Counter Clockwise

**CW**

Clockwise

**ODE**

Ordinary differential equation

**AR**

Aspect Ratio

**COTS**

consumer off the shelf

**GNC**

Guidance, Navigation and Control system

# Chapter 1

## Introduction

### 1.1 Research objectives

Thanks to technological development in the last decades, the presence of space agencies in space increased. Nowadays it's possible to explore space bodies with different approaches, which can be classified into seven groups including Earth-based observations, airborne and orbital telescopes, probes and fly-by spacecraft, orbiters, landers, rovers, and sample return [1]. The attention of space agencies has particularly focused on our solar system, which has four inner planets, four gas giant planets and 66 moons in total. Of these moons, one has atmosphere, 16 have water, ice or ocean, and 5 with both atmosphere and water or ice [1]. The presence of atmosphere on some planets and moons have inspired a new approach to space bodies exploration: aerobots. These new concept vehicles have the ability to explore greater ranges than rovers or landers. Also, these flying vehicles due to their proximity to the planet's surface could provide more high resolution information compared to the orbiters [1]. Aerobots include fixed, rotary and flapping wings drones, aerial balloons and Lighter-Than-Air vehicles (LTA). They can be applied to explore, characterize, and determine potential human landing sites [1] and help future astronauts in the exploration of a planet. Another application of some of these vehicles is to perform an autonomous precise landing of rovers or landers, which are also known as Precise Aerial Delivery Systems (PADS).

However, not all the planets and moons of our solar system containing an atmosphere are good candidates for aerobots: some of them have a too thin atmosphere, some don't have a surface and some have too much strong winds. In practice only three of them are appropriate: Mars, Venus and Titan.

In the last decades Mars has raised more and more interest in the scientific community and in various space agencies. Aerobots, in particular Unmanned Aerial Vehicles (UAVs), are increasingly more considered as valuable platforms for

planetary exploration. In this thesis two different types of UAVs are presented for a mission on Mars: a quadcopter drone and a parafoil system. These UAVs have very different characteristics and purposes. The drone is an optimal platform for the exploration of hazardous sights for common rovers, like caves or deep craters. While the parafoil system is a PADS that can be used to perform precise rover landings.

Some studies, like Ref. [2], proposed to use a parafoil system for an autonomous landing of high altitude radiosondes on Earth. Moreover in Ref. [3] an autonomous landing on Titan with a parafoil is discussed. Even if Mars has a thinner atmosphere, this aerobot could be suitable to perform an autonomous precise rover landing.

The aim of this thesis is to study and evaluate the feasibility of these two aerobots for a mission on Mars: the quadcopter drone and the parafoil system, with a focus on this last platform. A simplified dynamics model is used to represent the quadcopter, which doesn't describe the behavior of the actuators and neglects the aerodynamic drag acting on the body. To describe the parafoil's behavior a 6 DoF dynamics model is used, which consider the parafoil and the payload as a single rigid body with the body frame centered in the Center of Mass (CoM) of the canopy. Adding a Mars environment model, a 6 DoF dynamics simulator for both aerobots have been developed using MATLAB-Simulink, but in this thesis only the parafoil's simulator is presented. The drone's simulator structure is discussed in the Appendix A.

The parafoil's dynamics simulator has been designed to verify if a parafoil system is capable of executing a rover's autonomous landing with a low dispersion error. A configuration study of the parafoil is performed, to obtain a good gliding ratio, for reaching landing sites far from parafoil's deployment area. Moreover, a Simulink model is developed to analyze the behavior of the system in the martian atmosphere, studying a very simple possible trajectory. This consists of a linear approach with the highest gliding ratio, followed by a spiral descent over the landing site, which is the *Gale Crater* for this study. In addition, the possible wind disturbances in this region that could affect the flight is modeled as an oscillation around an average value taken from the Mars Climate Database [4].

To perform the planned trajectory autonomously, a Guidance, Navigation and Control (GNC) system is also considered. The guidance and control law inside the GNC system, is based on the method presented in Ref. [5], in which the angle between the heading vector of the parafoil and the direction to the target generates a yaw rate command, followed by a control law based on the angular velocities of the system. The parafoil system is also tested with wind disturbance to verify the robustness of the chosen control law. The results show that the implemented controller manages satisfactorily the aerobot, which is capable of properly following the assigned trajectory.

## 1.2 Possible target planets

There is evidence that many space bodies in our Solar System have atmosphere. The atmospheric characteristics of these solar bodies usually are different regarding their size, distance from the Sun, gravity, the type of gases, etc. [1]. The majority have an extremely thin atmosphere, like Earth's Moon, Io, Ganymede, Europa, Callisto and other natural satellites. Uranus, Saturn and Jupiter don't have a solid surface were to land and a dense atmosphere with strong winds. Pluto and Neptune have extreme atmospheric conditions as well. Only three solar bodies have good atmospheric conditions for flying vehicles: Venus, Saturn's satellite Titan and Mars. These bodies are good candidates, but have very different features between them, which define different design requirements.

### 1.2.1 Venus

Venus is an interesting target for scientific community: knowing its evolution could help understand how Earth-like planets evolve, although it's not suitable for human life.

Venus is extremely hot and has an atmospheric pressure on the surface 92 times higher than Earth atmosphere. The atmosphere mostly consist of carbon dioxide, a greenhouse gas, for this reason the mean surface temperature is 735 K. Another feature of the planet are the strong winds, with speeds that reach up to 85 m/s.

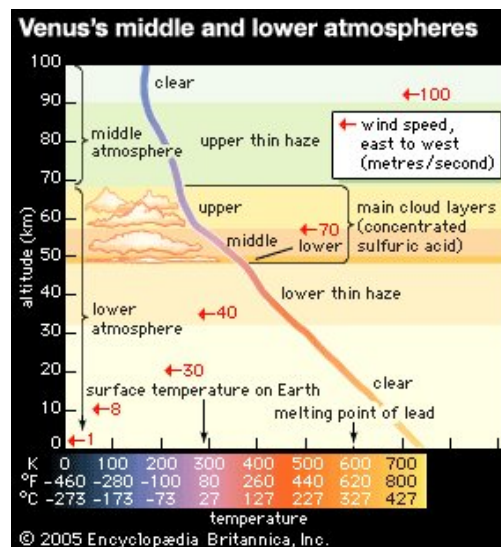
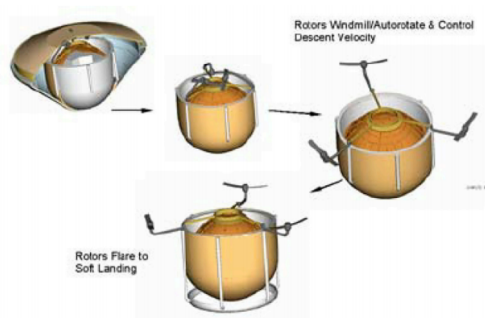
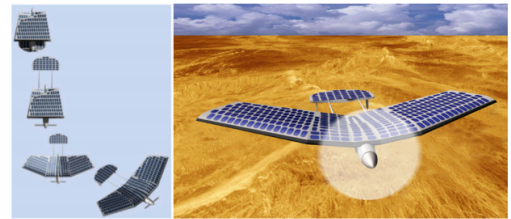


Figure 1.1: profile of Venus's atmosphere, Image credits: Encyclopædia Britannica

The troposphere begins at the surface and extends up to an altitude of 65 km. Therefore, in Venus, from an altitude of approximately 45 km, where the pressure is 2 bars, the temperature is 80 °C, and wind speed is about 45 m/s, to approximately 60 km, where the pressure is 0.2 bars, the temperature is -35 °C, and wind speed is 100 m/s [1]. In this region it's possible to design a drone capable of flying on Venus, due to the Earth-like atmospheric pressure. Furthermore Venus has a higher value of solar intensity compared to Earth. For this reason some balloons, airships and solar drones were designed in the past years, with the intention of remaining over 60 km of altitude for a long period of time. Other studies proposed to use rotorcrafts for atmospheric entry probe deceleration, due to the higher values of atmospheric density, which allows the use of small rotors for this purpose.



**Figure 1.2:** rotary wing decelerator for Venus probe by Young [1]



**Figure 1.3:** Solar Venus drone designed by Landis [1]

## 1.2.2 Titan

Saturn's moon Titan is likely the richest laboratory in the solar system for studying prebiotic chemistry, which makes studying its chemistry from the atmosphere to the surface one of the most important objectives in planetary science. Studying Titan's organic chemistry requires landing to sample and analyze fluids, dissolved species, and sediments from Titan's seas, lakes, tidal pools, or shorelines [3]. It is the second largest satellite in the solar system and its atmosphere consist of nitrogen (98.4%), methane (1.6%) and other gases. Therefore, Titan's atmosphere is denser than Earth's atmosphere, with a surface pressure of 147 kPa [1] and a mean surface temperature of 94 K, and 60 m/s winds speed.

In the last years different UAVs were proposed for the exploration of Titan: a balloon concept and a rotorcraft drone. These UAVs enable the study of large areas of the surface.

Another LTA vehicle could be used on Titan: a parafoil system. Landing dispersions with existing technology are hundreds of kilometers wide [3], therefore reduce this

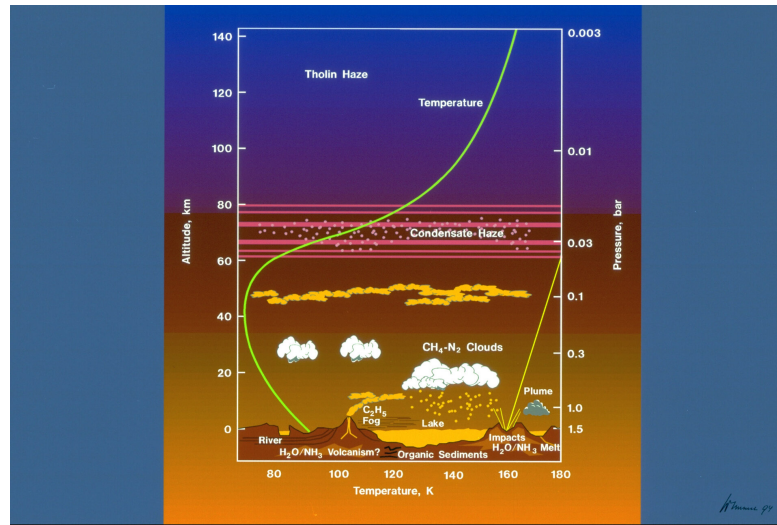


**Figure 1.4:** Titan's atmosphere profile, Image credits: ESA

dispersion is a big issue. The parafoil system, thanks to its controllability and lightness, its a promising concept to solve this problem; for Titan landings, but also for Mars.



**Figure 1.5:** Titan's drone concepts: Dragonfly and Montgolfiere balloon flagship [1]

### 1.2.3 Mars

The scientific community has supposed that Earth and Mars have been relatively similar worlds in the past. For this reason the red planet has aroused more and more attraction from space agencies, which have visited it several times in the past 50 years with rovers, probes, orbiters and landers. As said before, in recent years the idea of exploring Mars with aerobots has attracted lots of attention, for this reason the Red planet is the chosen target for our study.

**Table 1.1:** comparison between Earth and Mars

	Earth	Mars
mass ( $10^{24}$ kg)	5.97	0.64
volume ( $10^{10}$ km <sup>3</sup> )	108.3	16.3
average distance from Sun ( $10^6$ km)	149	228

Mars atmosphere is very thin and dusty and mainly composed of carbon dioxide [1] (96%) and some traces of argon, nitrogen, water and oxygen. The average surface pressure is between 0.4-0.87 kPa, which is similar to Earth's atmospheric pressure at 30.5 km altitude. Mars has four seasons like Earth and temperatures vary from  $-140^{\circ}\text{C}$  in winter, to  $20^{\circ}\text{C}$  in summer, while winds speed can vary from 2-7 m/s during summer to 17-30 m/s in a dust storm as reported on [6].

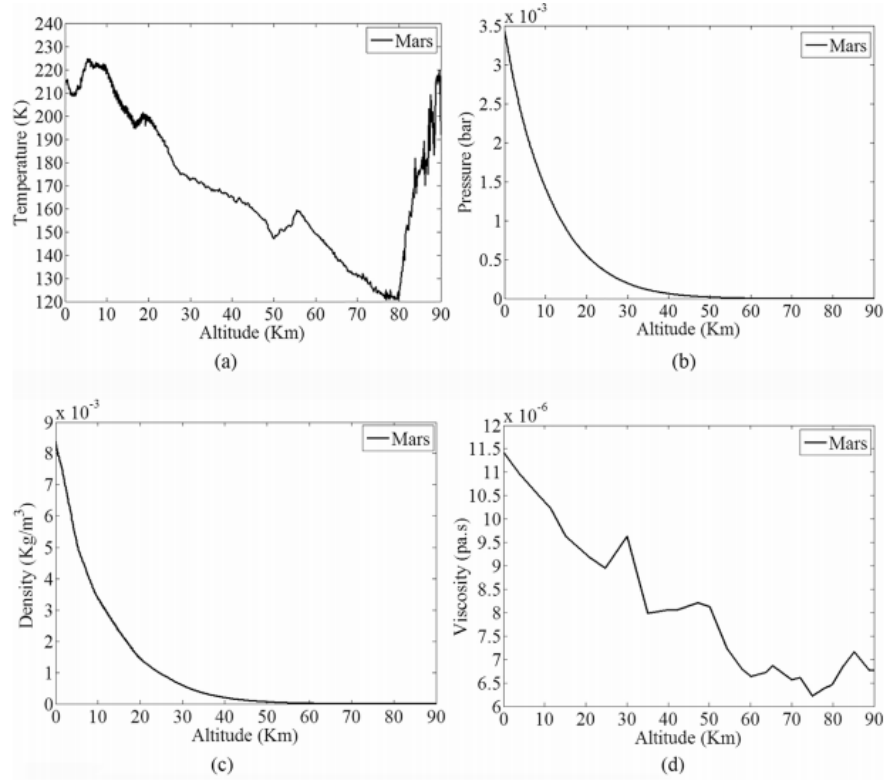


**Figure 1.6:** average (a)temperature, (b)pressure, (c)density, (d)viscosity of Mars atmosphere versus altitude [1]

Flying on Mars is an immense challenge: the Reynolds number of drones are on scale of  $10^5$ , while on Earth are on scale of  $10^6$ , due to its lower atmospheric

density. The speed of sound is 20% lower than on our planet, so it's easier to reach transonic velocities and generate destructive shock waves on the body, wing or propellers of the aerobot. Moreover, due to low percentage of  $O_2$  in the martian atmosphere, conventional combustion propulsion systems, such as oxygen-breathing motors and engines cannot be implemented on martian drones. Therefore, martian drones propulsion systems would rely on electrical or chemical systems [1]. These limitations have many implications on the design of a martian flying vehicle. In the following section some types of Mars flying vehicle concepts are presented.

### 1.3 Mars aerobots background

As reported before, aerobots can fulfil several exploration goals: exploring rough terrain for rovers and landers, offer high resolution images of landscape, soil composition analysis of large areas with gamma ray spectrometers or other techniques, magnetism analysis around geological features, offer a more precise landing of probes.

The design of a martian aerobot depends both on the atmospheric features of the planet and the mission objectives. Therefore very different aerobots concepts have been designed, which can be gathered in four categories: fixed wing, rotary wing, LTA vehicles and flapping wings.

#### 1.3.1 Fixed-wing

Due to the low density of the martian atmosphere and the low Reynolds number, fixed-wing drones should fly at very high speed, on the order of 0.6 Mach, and have a large wing area to generate the required lift force. If the drone is powered with propellers, these should be large and could not rotate too fast, for the same reasons. For fixed wing drones, the required lift coefficients to operate on Mars and Earth can be compared as follows:

$$\frac{C_{LM}}{C_{LE}} = \frac{W_M \rho_E S_E V_E^2}{W_E \rho_M S_M V_M^2} \quad (1.1)$$

where  $W$ ,  $\rho$ ,  $S$  and  $V$  represent the weight, density, wing area and flight speed, respectively on Mars with index  $M$ , and Earth with index  $E$  [1]. Since Mars gravity is 1/3 of Earth's gravity,  $W_M/W_E \simeq 1/3$ . In addition it's known that  $\rho_E/\rho_M \simeq 60$ . Applying these ratios in Eq. 1.1, one obtains:

$$\frac{C_{LM}}{C_{LE}} \approx 20 \frac{S_E V_E^2}{S_M V_M^2} \quad (1.2)$$

In Eq. 1.2 it can be seen that drones in Mars environment need a lift coefficient 20 times greater than on Earth, for the same given wing area and flight speed.

Otherwise it could be increased the wing area or the flight speed to increase the lifting force.

Existing airfoils provide maximum  $C_L$  values of  $\sim 2$ , therefore new airfoil shapes should be designed for flying on Mars. Drones with large wing area might need to utilize a folding scheme to fit inside the aeroshell used for the planetary entry phase. Moreover, high flight speeds causes some difficulties and complexities for landing, take-off and power requirements. Thus, the designed drone for Mars exploration can perform a single cruise flight [1].

An example of Mars fixed-wing drone is the *ARES-2* project proposed by NASA Langley Research center and JPL. *ARES-2* science objectives required completion of a 500-km pre-planned science survey from a vantage point 1-2 km above the surface terrain. During this traverse, unique measurements of the Mars atmosphere, surface and the interior would be obtained using magnetometers, a mass spectrometer, a point spectrometer, and imaging cameras [7]. The airplane was designed with a folding scheme to fit inside the aeroshell and deploy at an altitude between 2-3 km.

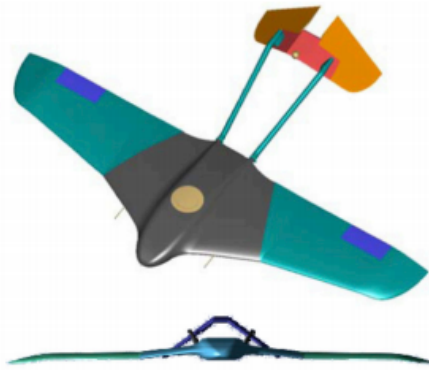


**Figure 1.7:** ARES-2 configurations for Mars exploration [1]

**Table 1.2:** ARES-2 Mars drone parameters

ARES-2 parameters	
wingspan	6.25 m
wing area	7 m <sup>2</sup>
overall length	4.4 m
overall height	0.7 m
reference chord	1.25 m
aspect ratio	5.58
wing sweep	30°/13°
cruise speed	145 m/s
mass	175 kg

As reported in Table 1.2 *ARES-2* has a high cruise speed and large wing area, thus a soft landing in a short range is quite impossible for this type of vehicle. Since the objective of this thesis is to perform a precise autonomous landing for a rover, another aerobot has been selected, lighter and easier to store inside an aeroshell: the parafoil system.

### 1.3.2 Rotary-wings

Rotary wing drones can perform vertical take-off, landing, and hovering flight in different solar bodies [1], enables remote-site sample return to landers with precision placement, have greater range of exploration than rovers. For these reasons these

platforms are considered the most suitable configurations for Mars exploration, although drone’s propellers have low performance in the thin Mars atmosphere. Limitations on the propellers of these types of drones are various: the rotational speed should be lower and the radius higher than on Earth, due to the lower atmospheric density and lower speed of sound. Moreover the low temperatures on the planet are a problem for electrical driven motors: battery performance decrease considerably at low temperatures. Rotorcrafts can have different capabilities and advantages according to their size, as reported in the Table 1.3.

**Table 1.3:** Merits and Limitations of Large and Small Mars Rotorcrafts [8]

Small Rotorcraft	Large Rotorcraft
<i>Capabilities</i>	<i>Capabilities</i>
<ul style="list-style-type: none"> <li>• Perform efficient short- and mid-range “low and slow” aerial surveys</li> <li>• Take off and land at remote unprepared sites</li> <li>• Drop small probes and sensors and/or acquire small samples of soil and rocks</li> <li>• Act as advance scouts for human explorers or large robotic rovers</li> <li>• Act as, or transport and install, telecom and data relays</li> <li>• Perform high-risk and/or “expendable” tasks</li> </ul>	<ul style="list-style-type: none"> <li>• Can carry more sophisticated instrument packages than smaller platforms</li> <li>• Greater range than smaller platforms</li> <li>• Medium size high-value payloads point to point</li> <li>• Possibly act as a short to mid-range “manned” transport platform</li> </ul>
<i>Advantages</i>	<i>Advantages</i>
<ul style="list-style-type: none"> <li>• One or many Mars rotorcraft working together in concert</li> <li>• Almost de facto robotic symbiosis of small rotorcraft working with other robotic/automated systems</li> </ul>	<ul style="list-style-type: none"> <li>• In general, at most, one or two larger rotorcraft work together to perform tasks</li> <li>• Larger rotorcraft would be used for campaigns leading up to and including human exploration</li> </ul>
<i>Disadvantages</i>	<i>Disadvantages</i>
<ul style="list-style-type: none"> <li>• Range limited for small platforms to an operational radius of less than 50km</li> <li>• Relatively high energy expenditure for a robotic asset, but not too high as compared to other equipment required for human exploration of Mars</li> </ul>	<ul style="list-style-type: none"> <li>• Range for larger vehicles increases to an operational range of a couple hundred kilometers</li> <li>• Larger rotorcraft consume large quantities of energy; however, compared to energy requirements for ISRU for return-to-Earth propellant, or human habitat and base camp power needs, then energy levels required are not too excessive</li> </ul>

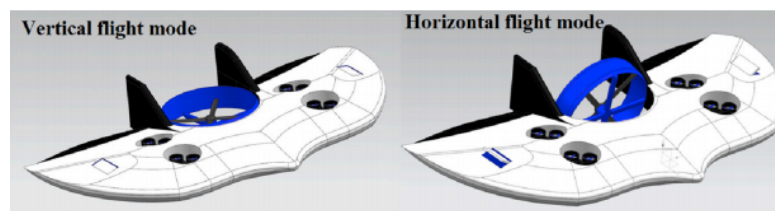
An example of small Mars rotorcraft is NASA’s *Mars helicopter Ingenuity*, landed in these months on Mars along with *Perseverance* rover. This drone is a coaxial autonomous helicopter, and the project is solely a demonstration of technology; it is not designed to support the *Mars 2020/Perseverance* mission [9]. As one can see in Table 1.4, the drone’s weight is quite low and the rotor system span is high. Although this configuration allows to have a compact and light drone, in this thesis a different architecture is presented: a quadcopter. Such configuration is equally light, but less compact and has the advantage of having a simpler dynamics model, that makes this architecture the best for a preliminary design.

**Table 1.4:** Mars Ingenuity features, reported on [9]

Ingenuity features	
Height	0.49 m
Rotor system span	1.2 m
Weight	1.8 kg
energy	Solar-powered and recharges on its own
rotors rotational velocity	2400 rpm

**Figure 1.8:** Representation of Mars Helicopter Ingenuity on the surface of Mars [9]

Others rotary-wing drones are tilt-rotors, tilt-wing and tilt-body drones, which can be considered as the future of space drones configurations. Applying a rotating propulsion system on a flying wing can provide all the advantages of a fixed wing with forward flight and a rotary wing drone with hovering capabilities [1]. The disadvantages of these drones is that with even relatively small "gross weight" masses will likely require astronaut assembly, because of the large wing surfaces entailed by these vehicles [8].

**Figure 1.9:** A schematic view of a flying wing with vertical and horizontal flight modes [1]

### 1.3.3 LTA vehicles

Balloons, airships, parafoil and parachute are all different types of LTA vehicles. Balloons and airships are flying configurations which had important role during space exploration in the past decades. A flying balloon needs simple technology to be designed and manufactured. In addition to that, it does not need power to maintain the altitude. These flying objects apply power only for instruments and payloads. They can change their altitude but they are not able to change their location. Balloons cannot stay in the Sun or keep their station and they do not have enough flexibility for atmospheric science. Airships compared to balloons have difficulty to stow and deploy. They are able to change their altitudes with slow speed. Same as balloons, airships cannot stay in Sun and keep their station, and they have too much complexity and too low flexibility[1].

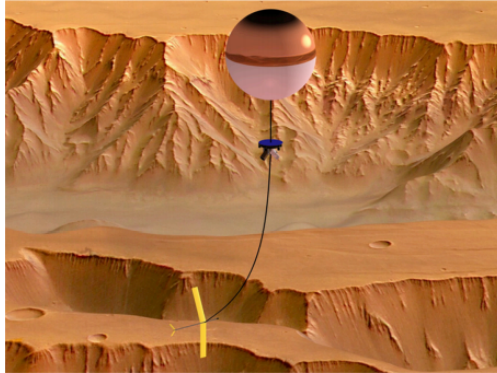


**Figure 1.10:** View of designed and manufactured Balloon Guidance System [1] for Mars exploration

The parafoil system, also called ram-air parachute, like others LTA vehicles is flexible and easy to design and manufacture, but is more controllable and have high glide ratios, which make it perfect to perform an autonomous precise landing on the surface of Mars. Parafoils have a ram-air inflated, double membrane airfoil cross section and are equipped for steering by means of wing tip or trailing edge lines [3]. Pulling the lines creates a difference of angle of attack at the wing tips, therefore different drag forces which generate a yaw moment. This technology is widely used on Earth already, some studies proposed to use this technology to land on Titan, as reported on [3], and the aim of this thesis is to demonstrate that could also be used for an autonomous rover landing on Mars.



**Figure 1.11:** Parafoil model. Credits: free3D.com

### 1.3.4 Flapping-wings

In recent years flapping winged aerobots for autonomous flight on Mars have been proposed. This innovative solution is based on the capability to generate high lift under low Reynolds number flight flapping the wings. This is possible due to the fact that a wingspan of 1 m on Mars operates with a similar Reynolds number of an insects on Earth. However these drones have an endurance problem [1], they require lot of power to fly, so they can be applied only in short range missions. Furthermore so far only allometric formulae extracted from natural birds and insects [1] were used to design flapping wings. Therefore, these empirical formulas should be revisited and modified, to optimize this configuration for the martian environment.

An example of flapping wing drone is the *Entomompter* designed by Colozza and shown in Figure 1.12.



**Figure 1.12:** View of Entomompter designed by Colozza [1] for Mars exploration

# Chapter 2

## Mathematical models

In this chapter the main features of the system and the environment in which it operates are presented. In fact, careful observation and study make possible to model apparently complex physical phenomena in mathematical equations that can be resolved.

### 2.1 Mars environment

In this section the Martian environment is presented in general. In particular, all those aspects that affect flight are highlighted. Mars is a cold, dry and dusty planet and, like the Earth, it rotates on itself and around the Sun; this results in the cyclical repetition of the seasons, which have very different durations due to the high eccentricity of the planet's orbit [10].

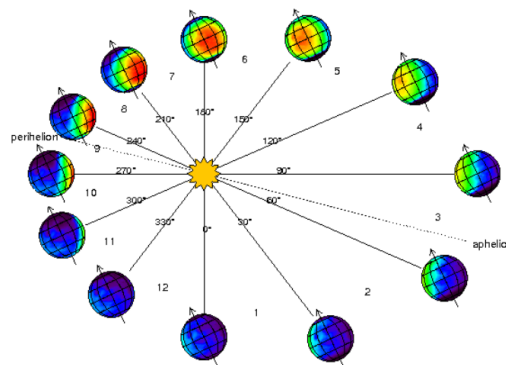


**Figure 2.1:** Illustration of Martian Solar Longitude Diagram (Mars Climate Database, 2014)

The seasonal conditions, together with strong wind gusts, atmospheric density

and temperature are the main factors influencing flight. Severe storms can be so dusty that only 5% of the light reaches the surface, causing the solar cells to malfunction and mechanical components to fail [11]. For this reason it is necessary to avoid them by selecting an appropriate time of year and it is preferable to conduct the mission during the late spring and early summer periods because of the volatile weather in winter. Excluding heavy storms, flying on Mars would seem to be easier since the gravity is a third of that on Earth. In reality, the low atmospheric density makes it very difficult. Lift and thrust, in fact, are directly related to density by the following formulas:

$$L = \frac{1}{2}\rho V^2 C_L S \quad (2.1)$$

$$T = \frac{1}{2}\rho V_{tip}^2 C_T A \quad (2.2)$$

Where  $L$  is the lift force,  $\rho$  is the atmospheric density,  $V$  is the air speed,  $C_L$  is the coefficient of lift for the vehicle,  $S$  is the reference surface area,  $T$  is rotor thrust,  $C_T$  is the coefficient of thrust,  $A$  is the area of the rotor, and  $V_{tip}$  is the speed of the rotor tip [10]. As the density is a hundred times lower than on Earth, generating thrust is much more difficult. This implies that aircraft generally have larger dimensions and heavier weights than those on the ground. For greater understanding, the main parameters influencing flight are listed below:

**Table 2.1:** Comparison of Relevant Earth and Mars Parameters [10]

	Earth	Mars
Gravity (m/s <sup>2</sup> )	9.81	3.71
Atmospheric Composition	N <sub>2</sub> 78.08%	N <sub>2</sub> 2.7%
	O <sub>2</sub> 20.95%	O <sub>2</sub> 0.13%
	H <sub>2</sub> O 0.4 %	CO 0.08 %
	Ar 0.93%	Ar 1.6%
	CO <sub>2</sub> 0.036%	CO <sub>2</sub> 95.32%
Atmospheric Density (kg/m <sup>3</sup> )	1.225	0.0138
Average Temperature (K)	288.15	210.15
Average Wind Speed (m/s)	0 - 100	2 - 30 (dust storm)
Speed of Sound (m/s)	340.3	245
Dynamic Viscosity	1.789 x 10 <sup>-5</sup>	1.2235 x 10 <sup>-4</sup>

As can be seen from the low average temperature and atmospheric composition, the speed of sound on Mars is lower than on Earth. This leads to a higher rotor

tip Mach number, in the case of rotors. Indeed:

$$M_{tip} = \frac{V_{tip}}{\sqrt{\gamma RT}} \quad (2.3)$$

Where  $M_{tip}$  is the rotor tip Mach number,  $\gamma$  is the ratio of specific heats of the gas,  $R$  is the molar gas constant, and  $T$  is the temperature of the air. It is easy to understand how this limits the angular speed of the propellers and therefore also the maximum thrust that can be generated. This results in constraints that must be satisfied and which heavily influence the physical model of the aerobots. The Figure 2.2 shows the variation of thrust as the Mach at tip varies on Earth and Mars.

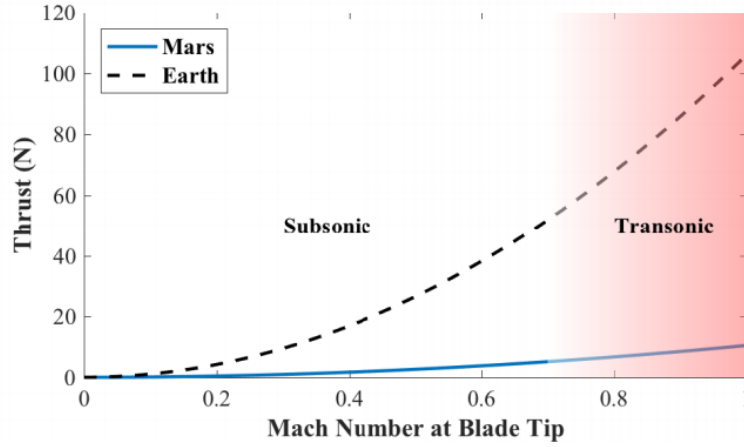


**Figure 2.2:** A Comparison of Rotor Thrust Generated on Earth and Mars[10]

Like the rotors, flying vehicles also have problems linked to the environment; the same amount of  $CO_2$  is not present on Earth as on Mars. Because of this, the 'Red Planet' has a higher dynamic viscosity, which implies lower Reynolds numbers described by the Equation 2.4.

$$Re = \frac{\rho V L}{\mu} = \frac{V L}{\nu} \quad (2.4)$$

Where  $Re$  is the Reynolds number,  $\mu$  is the dynamic viscosity,  $\nu$  is the kinematic viscosity, and  $L$  is the reference length. For comparison, aircraft flying in this Reynolds number regime on Earth include small Unmanned Aerial Vehicles (UAV) and Micro Air Vehicles (MAV) [12].

In view of this, it is necessary to study these effects well and recreate models of them as faithfully as possible.

## 2.2 Reference frame

In this section the reference systems that are used below and the mathematical operations to bind the state variables in the different reference frames are discussed for greater clarity.

### 2.2.1 Mars Inertial Frame

The Martian Inertial frame (MI) is a North-East-Down frame with the  $x$  and  $y$  axes lying on the local martian horizontal plane with the origin at the aerobot's CoM. The  $x$  axis is aligned with local martian North and the  $y$  axis is aligned with local martian East, while the  $z$  axis is oriented to form a right-handed triad. Values described in the MI frame are denoted  $[ \ ]_I$  [10].

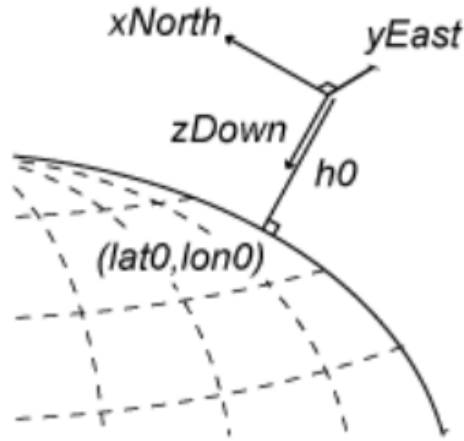
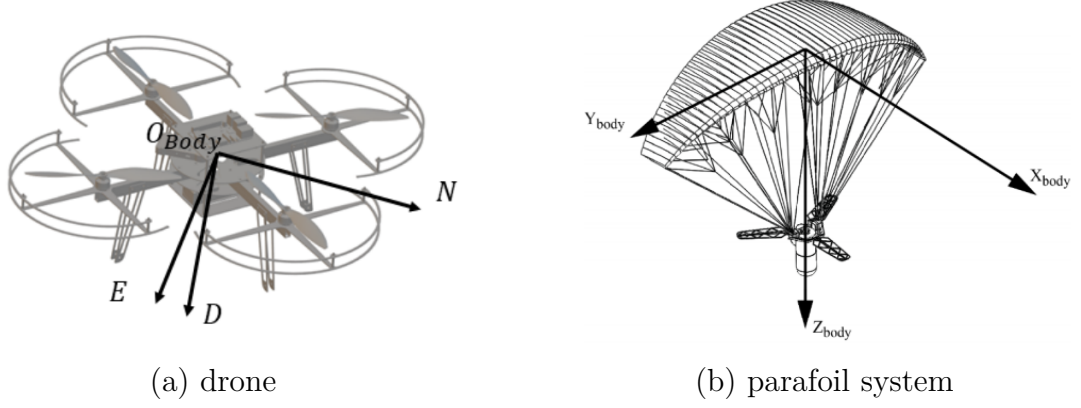


Figure 2.3: Mars Inertial Reference System

### 2.2.2 Body Frame

The body frame is fixed to the aerobot with its origin at the aerobot's CoM. The  $x$  axis is aligned with the aerobot's nose. The  $z$  axis points down through the center of the drone opposite to the rotor plane in the case of the drone, while it is directed along the joint of the centres of mass between the wing and the payload, towards the latter, in the case of the parafoil. Finally, the  $y$ -axis is directed to form a right-handed orthogonal triad. Values described in the body frame are denoted  $[ \ ]_B$  [10].



**Figure 2.4:** Body Reference Frame for drone and parafoil system

It's possible to switch from one reference system to another using the appropriate rotation matrices:

$$\mathbf{R}_I^B = \mathbf{R}_1(\phi)\mathbf{R}_2(\theta)\mathbf{R}_3(\psi) \quad (2.5)$$

$$\mathbf{R}_B^I = (\mathbf{R}_I^B)^T = \mathbf{R}_3^T(\psi)\mathbf{R}_2^T(\theta)\mathbf{R}_1^T(\phi) \quad (2.6)$$

$\mathbf{R}_I^B$  is used to switch from the MI system to the body's one, where  $\phi$  is the roll angle,  $\theta$  is the pitch angle and  $\psi$  is the yaw angle. Each angle indicates the rotation to perform to align the two reference frames. The rotational matrices are defined as:

$$\mathbf{R}_1(\phi) = \begin{bmatrix} 1 & 0 & 0 \\ 0 & \cos(\phi) & \sin(\phi) \\ 0 & -\sin(\phi) & \cos(\phi) \end{bmatrix} \quad (2.7)$$

$$\mathbf{R}_2(\theta) = \begin{bmatrix} \cos(\theta) & 0 & -\sin(\theta) \\ 0 & 1 & 0 \\ \sin(\theta) & 0 & \cos(\theta) \end{bmatrix} \quad (2.8)$$

$$\mathbf{R}_3(\psi) = \begin{bmatrix} \cos(\psi) & \sin(\psi) & 0 \\ -\sin(\psi) & \cos(\psi) & 0 \\ 0 & 0 & 1 \end{bmatrix} \quad (2.9)$$

## 2.3 Gravity model

Gravity on Mars is about one third of that on Earth, as mentioned above. Due to Mars' ellipsoid shape the gravitational acceleration is not uniformly distributed over the planet, being particularly intense at the poles. There are kilometer level resolution models that allow us to observe how gravity varies on the planet's surface [13].

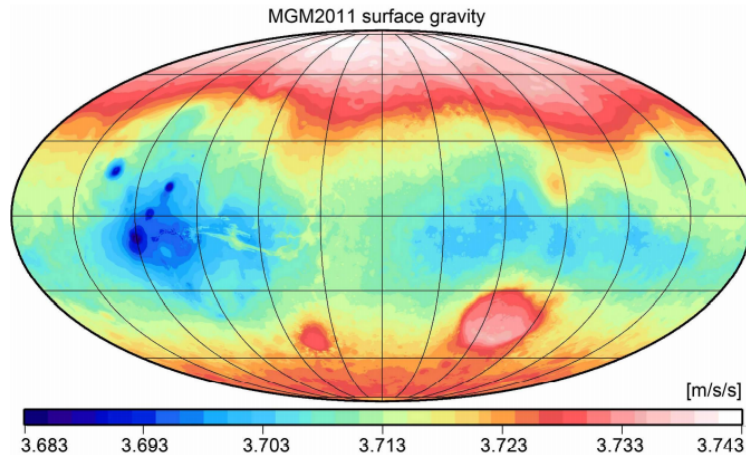


**Figure 2.5:** Global Gravity Map of Mars [13]

As can be seen from the graph, the variation of gravitational acceleration is not such as to significantly affect the dynamics of an aerobot, so we can assume the gravity acceleration as a constant  $g = 3.72 \text{ m/s}^2$ . In particular, in the developed model, the force generated by gravity is expressed in a NED system:

$$\vec{F}_g = \begin{bmatrix} 0 \\ 0 \\ mg \end{bmatrix}_I \quad (2.10)$$

However, for the calculations carried out, it is necessary to relate the force in body axes through the appropriate rotation matrices, obtaining:

$$\mathbf{R}_I^B \vec{F}_g = \begin{bmatrix} -mg \sin(\theta) \\ mg \cos(\theta) \sin(\phi) \\ mg \cos(\theta) \cos(\phi) \end{bmatrix} \quad (2.11)$$

## 2.4 Atmosphere model

The Martian atmosphere consists of a thin layer of gas, it is not uniform and the properties of the fluids change as a function of time and the geographical area selected. However, the main variations depend on the altitude in relation to the Martian soil itself. In particular, the Sun heats the surface and part of this heat is transmitted to the gas near the surface which is then diffused or convected up through the atmosphere. Thus, the gas temperature is higher near the surface and decreases as we increase altitude. Furthermore, as with the Earth, the pressure of the atmosphere decreases with increasing altitude while the density depends on the first two factors mentioned.

In order to perform simulations and understand the variation of these parameters, the Mars Global Surveyor developed a model in April 1996. Information on the Martian atmosphere was collected by Jonathon Donadee of Canfield (Ohio) Middle School during a cyber-mentoring programme in 1999. The model has two zones with separate curves suitable for the lower and upper atmosphere. The lower atmosphere runs from the surface of Mars to 7,000 meters [14].

$$T [C^\circ] = \begin{cases} -31 - 0.000998h, & \text{if } h \leq 7000m \\ -23.4 - 0.00222h, & \text{if } h > 7000m \end{cases} \quad (2.12)$$

$$p = 0.699e^{-0.00009h} [kPa] \quad (2.13)$$

$$\rho = k \left( \frac{p}{0.1921(T + 273.1)} \right) \left[ \frac{kg}{m^3} \right] \quad (2.14)$$

Where the parameter  $k$  depends on the chosen geographical area, the time and the period of the year. While the value 0.1921 is the specific gas constant  $\bar{R}$  is expressed as  $kJ/(kg K)$ .

The model, clearly, could be replaced by a more accurate one in the future, but for a preliminary analysis it is quite accurate.

## 2.5 Wind model

The atmospheric changes described above cause wind on Mars. It varies with the seasons, the time of day and even altitude. In order to understand its trend, reference was made to the Mars Climate Database. [4].

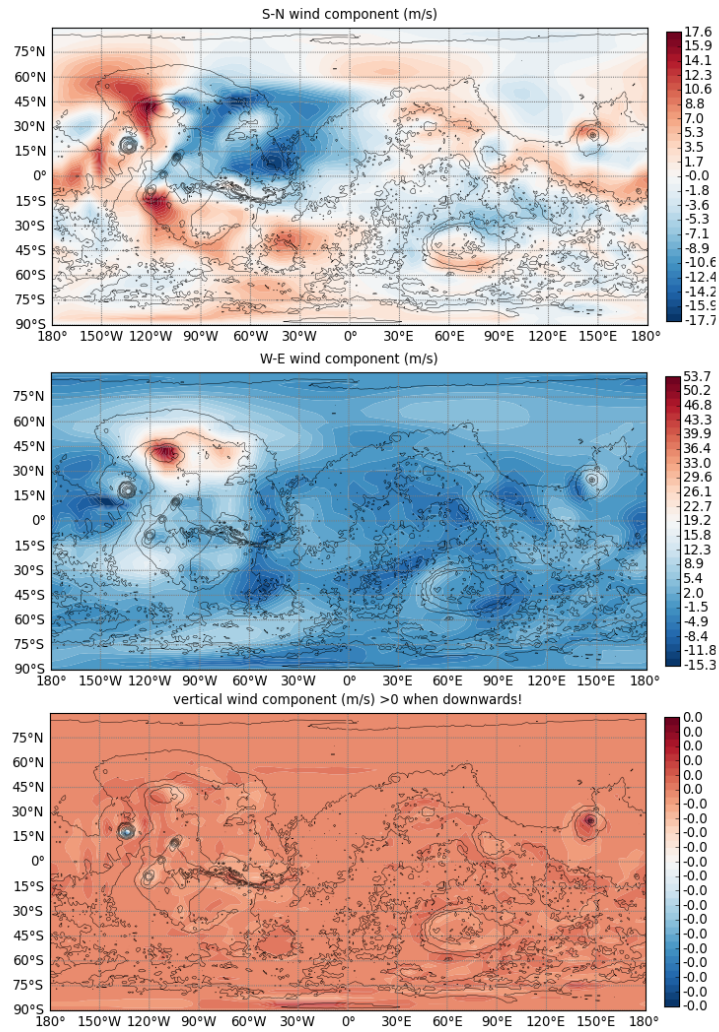


**Figure 2.6:** Average wind in Mars during winter at 10m altitude [4]

To create a functional model, it has been chosen to observe the wind trend in the 3 directions of the MI frame for different seasonal periods, assuming as landing point the *Gale Crater*, which is the same as *Curiosity*, then the 3 average components that best represent the wind trend have been chosen.

- **Wind in vertical direction:**  $2.3 \times 10^{-4}$  m/s
- **Wind in South/North direction:** 6.08 m/s
- **Wind in West/East direction:** 0.87 m/s

However, having a constant wind in modulus and direction is not a truthful representation of real conditions. However, having a constant wind in modulus and

direction is not a truthful representation of real condition. In such a case one could not evaluate the ability of the controller to react to a continuously varying and random perturbation. So a model is created where two disturbance components are added to a random constant component to recreate the wind behavior, in the following cases the value used is not one of the three previously chosen because the model works exactly in the same way a priori of the average value to which it is chosen to add the disturbances:

- the **Bias** is generated through an uniformly distributed random signal equal to  $\pm 10\%$  of average wind value, which changes at each integration step, so its frequency is equal to that of dynamics of the system;

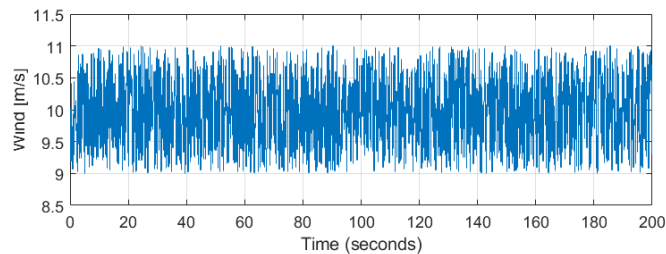


**Figure 2.7:** Average wind with Bias of 10%

- The **White Noise**: is added to the wind with bias is added an additional disturbance generated by a Gaussian distribution, like the previous one it works at the same frequency of the dynamics equations.

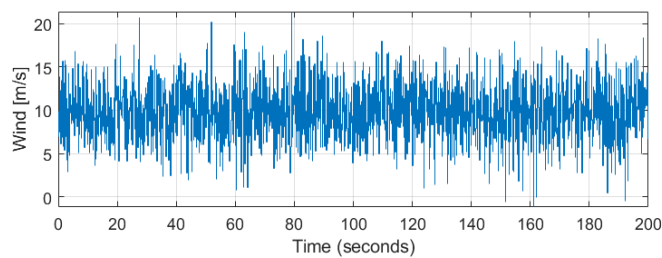


**Figure 2.8:** Average wind with Bias of 10% and Noise

The conceptual diagram of how the wind model works is shown in the Figure 2.9, where *Median wind* is a vector containing the 3 selected mean wind values.

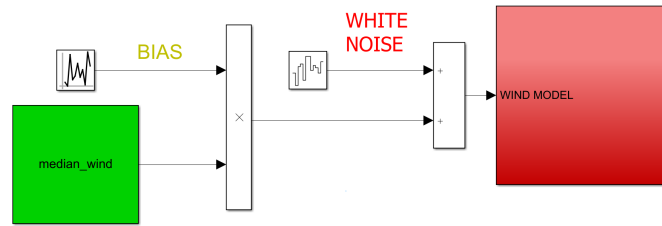


Figure 2.9: Wind model operating diagram

## 2.6 Drone's models

There are various configurations in which a multicopter can appear, each of which has its merits and demerits, as well as various mathematical models representing the evolution of its motion.

- **Bicopter's** composed by two rotors and for this reason is the least stable and is difficult to tune. It is also the one that produces the least lift in its category, in fact it has the fewest propellers [15];



Figure 2.10: Example of Bicopter

- **Tricopter** are considered the least expensive type of multirotor both because they have only three motors and because they require servo motors which are much less expensive than brushless motors. Another advantage is the wider angle (120 degrees) between the two front motors, which makes it easy to do in-air videography while the propellers remain out of sight. Typical rotor's configurations are "T" or "Y" shaped. Two propellers which are on the front arms pointed to the sides or slightly forwards, and one arm backwards. The latter can be rotated by means of a suitable bracket to control yaw. However, the major problem with this type is that, as with the bicopters, it is not capable of withstanding failure [15];



**Figure 2.11:** Example of Tricopter "Y" shaped

- **Quadcopter** consists of 4 rotors mounted on arms located in the same plane at 90 degrees to each other. There are two sets of Clockwise (CW) and Counter Clockwise (CCW) propellers mounted on the motors to create opposite force to balance it. The main advantages of quadcopters over other copters are that they do not require mechanical linkages to vary the rotor blade pitch angle as they stroll or spin. This makes design of quadcopter simple and stable. For the same lift generated, the quadcopter has rotors, each of which is smaller than that of a helicopter. This reduces the probability of damage as the centripetal force on each rotor is lower [15]. For this work, two different configuration are analyzed:

- *Quad + configuration* is the easiest to control; the rotor arms are arranged along the x,y body axes but in this case none of the directions of movement correspond to the focal axis of a possible optical system, since if this were the case the view would be obstructed by the rotors themselves;
- *Quad × configuration* is the most appropriate to support a payload to scan the environment; the rotor arms are arranged to form the bisectors of the x,y body axes.

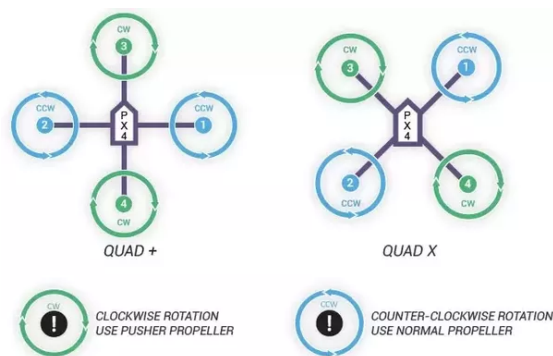


**Figure 2.12:** Example of Quadcopter "+" and "x" shaped

In this work the quadcopter  $\times$  configuration and the equations governing its motion are discussed. In particular, the evolution of the motion of this body is governed by kinematic and dynamic models.

### 2.6.1 Kinematics model

The kinematics model represent all those equations needed to move from one reference system to another. The main variables are:

- Euler angles and angular velocities in the inertial frame;

$$\dot{E} = [\dot{\phi}, \dot{\theta}, \dot{\psi}]^T \quad (2.15)$$

- Angular velocities in body reference frame.

$$\omega = [p, q, r]^T \quad (2.16)$$

In the subsection 2.2.2 is shown how to change the reference system; however the matrices presented permit changing the position coordinates but not the angular or translational velocities in the two references. For this reason it's necessary to find a relationship between the Euler angles characterizing the quadrotor attitude w.r.t. the inertial frame and the angular velocities  $p$ ,  $q$  and  $r$  in the body reference frame. It is obtained that:

$$\begin{bmatrix} \dot{\phi} \\ \dot{\theta} \\ \dot{\psi} \end{bmatrix} = \begin{bmatrix} 1 & s_{\phi}t_{\theta} & c_{\phi}t_{\theta} \\ 0 & c_{\phi} & -s_{\phi} \\ 0 & \frac{s_{\phi}}{c_{\theta}} & \frac{c_{\phi}}{c_{\theta}} \end{bmatrix} \begin{bmatrix} p \\ q \\ r \end{bmatrix} \quad (2.17)$$

Where:

$$\cos(\cdot) = c_{(\cdot)} \quad \sin(\cdot) = s_{(\cdot)} \quad \tan(\cdot) = t_{(\cdot)} \quad (2.18)$$

Furthermore, Euler angles are not the only set of coordinates for defining the drone orientation. In fact, when  $\theta = \pi/2$  or so, it is possible to encounter a numerical instability, the denominator of some elements of the above matrix goes to zero: this problem called *Gimbal Lock*. From a physical point of view it consists in the loss of one degree of freedom in a three-dimensional caused when the axes of two of the three gimbals are driven into a parallel configuration and it becomes impossible to distinguish them.

This is why quaternions are used. They haven't singularity and are defined as follows:

$$\mathbf{q} = q_0 + q_1\mathbf{i} + q_2\mathbf{j} + q_3\mathbf{k} \quad \text{with} \quad \mathbf{ijk} = 1 \quad (2.19)$$

Where  $q_0$  is a scalar value and  $q_1$ ,  $q_2$ ,  $q_3$  are the component of the vector  $\mathbf{q}$  However, quaternions have not been used in this discussion because the drone modeled here is unlikely to achieve such high attitude angles.

## 2.6.2 Dynamics model

The dynamics model describe the rotational and translational dynamics of the aerobot taking into account forces and moments generated by the motion of the rotors, aerodynamic forces and moments acting on the body, and any cross-coupling effects produced from the relative motion of the four rotors and body. To develop a simple model, however, simplifying assumptions must be made, in order to have second order ordinary differential equation (ODE) [16]:

1. The quadrotor and all its components (i.e. propellers, motors...) are considered as rigid bodies;
2. The quadrotor CoM is the origin of the body reference frame
3. The actuators are not modeled;
4. The aerodynamic forces are not considered;
5. The planet is considered as flat and its rotation is negligible w.r.t. body angular speeds.

Therefore, it is necessary to describe the translational and rotational dynamics:

- **Traslational dynamics** is based on Newton's Second Law

$$\mathbf{F} + \mathbf{R}_I^B m \mathbf{g} = m \left[ \frac{d\mathbf{v}_B}{dt} + \boldsymbol{\omega}_B \times \mathbf{v}_B \right] \quad (2.20)$$

Where:

- $v_B$  is the relative velocity of the quadrotor CoM w.r.t. air mass, defined

$$\text{as } \mathbf{v}_B = \begin{bmatrix} u \\ v \\ w \end{bmatrix}$$

- $\mathbf{F}$  is a vector containing the propulsive thrust given by rotors

$$- \boldsymbol{\omega}_B \times \text{ is defined as } \boldsymbol{\omega}_B \times = \begin{bmatrix} 0 & -r & q \\ r & 0 & -p \\ -q & p & 0 \end{bmatrix}$$

Explicitly expressing the acceleration from this formula, it is possible, by integrating it, to derive the speed of the drone

$$\dot{\vec{V}}_B = \frac{1}{m} \left( \begin{bmatrix} -mgs\theta \\ mgc\theta s\phi \\ mgc\theta c\phi \end{bmatrix} + \begin{bmatrix} F_X \\ F_Y \\ F_Z \end{bmatrix} \right) - \vec{\omega}_B \times \vec{V}_B \quad (2.21)$$

- **Rotational dynamics** is based on Euler's Rigid Body Equations

$$\boldsymbol{\tau} = \left( \frac{d\mathbf{H}}{dt} + \boldsymbol{\omega}_B \times \mathbf{H} \right) \quad (2.22)$$

Where

- $\boldsymbol{\tau}$  is a vector of the moment acting on the drone
- $\mathbf{H}$  is the vector containing the component of the angular momentum defined as

$$\mathbf{H} = \mathbf{J}\boldsymbol{\omega}_B = \begin{bmatrix} J_x & J_{xy} & J_{xz} \\ -J_{xy} & J_y & -J_{yz} \\ -J_{xz} & -J_{yz} & -J_z \end{bmatrix} \begin{bmatrix} p \\ q \\ r \end{bmatrix}$$

By making the angular acceleration explicit, it is possible to calculate the angular velocities of the drone in body axes by integrating them.

$$\dot{\boldsymbol{\omega}}_B = -\mathbf{J}^{-1} (\boldsymbol{\omega}_B \times (\mathbf{J}\boldsymbol{\omega}_B)) + \mathbf{J}^{-1}\boldsymbol{\tau} \quad (2.23)$$

## 2.7 Parafoil's models

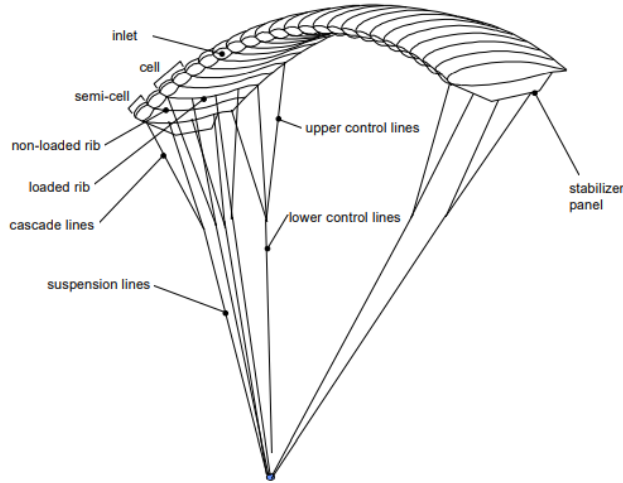


**Figure 2.13:** The ram-air parachute [17]

Several approaches can be used to describe the dynamics of a parafoil with a suspended payload. 3 to 6 DoF models use simplified aerodynamics (steady coefficients), constant drag area for payload, simplified added mass effects and two-dimensional wind models [2]. 9 to 15 DoF models are more accurate, but

require more accurate estimations of aerodynamic coefficients, lines elasticity and, eventually, joint or hinge modelling, if present [2]. In this section a 6 DoF model used to represent the parafoil system is discussed. It's a good compromise between computational complexity and accurate solutions. In this model parafoil and payload (vehicle) are considered to be a single rigid body. This assumption is reasonable if the parafoil is completely inflated and the suspension lines are completely stretched [2].

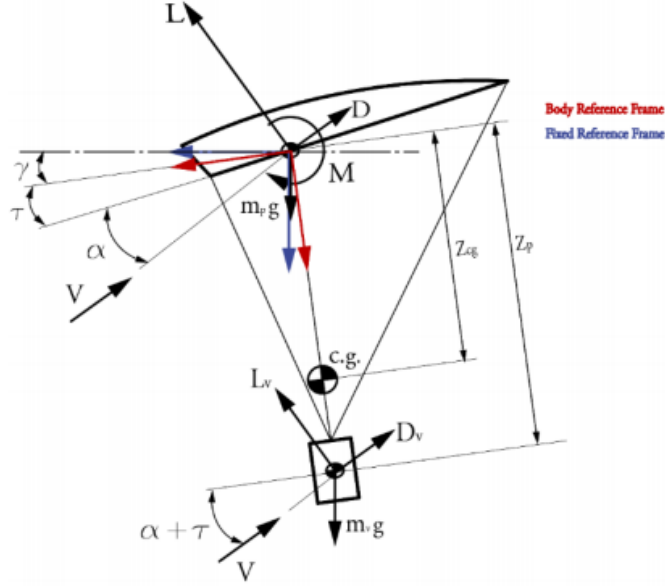


**Figure 2.14:** Free body configuration of the parafoil-payload system. Image from [2]

### 2.7.1 Kinematics model

The kinematics variables are three Euler orientation angles and three directional velocities, that can be represented in inertial and body frame:

$$V = [u, v, w]^T \quad \omega = [p, q, r]^T \quad (2.24)$$

$$\dot{N}_{av} = [\dot{x}_N, \dot{x}_E, \dot{h}]^T \quad \dot{\Phi} = [\dot{\phi}, \dot{\theta}, \dot{\psi}]^T \quad (2.25)$$

$V$  and  $\omega$  represent the velocity and angular velocity in the body frame, which is centered in the CoM of the parafoil, as presented in Figure 2.4(b). While  $\dot{N}_{av}$  and  $\dot{\Phi}$  are the velocity and angular velocity in the NED inertial frame. The variables in the two frames are linked to each other through the rotational matrix  $R_B^I$  (Eq. 2.6) and its derivative:

- **Navigation equations**

$$\dot{N}_{av} = \begin{Bmatrix} \dot{x}_{N'} \\ \dot{x}'_E \\ \dot{h} \end{Bmatrix} = [R_B^I] \begin{Bmatrix} u \\ v \\ w \end{Bmatrix} \quad (2.26)$$

- **Angular Kinematics equations**

$$\dot{\Phi} = \begin{Bmatrix} \dot{\phi} \\ \dot{\theta} \\ \dot{\psi} \end{Bmatrix} = [R_B^I]' \begin{Bmatrix} p \\ q \\ r \end{Bmatrix} \quad (2.27)$$

$$[R_I^B]' = \begin{bmatrix} 1 & 0 & -s_\theta \\ 0 & c_\phi & s_\phi c_\theta \\ 0 & -s_\phi & c_\phi c_\theta \end{bmatrix} \quad [R_B^I]' = \begin{bmatrix} 1 & t_\theta s_\phi & t_\theta c_\phi \\ 0 & c_\phi & -s_\phi \\ 0 & \frac{s_\phi}{c_\theta} & \frac{c_\phi}{c_\theta} \end{bmatrix} \quad (2.28)$$

Where:

$$\cos(\cdot) = c_{(\cdot)} \quad \sin(\cdot) = s_{(\cdot)} \quad \tan(\cdot) = t_{(\cdot)} \quad (2.29)$$

## 2.7.2 Dynamics model

In general, since the payload and parafoil are considered a single rigid body, the following equations can be applied:

$$\Sigma \begin{Bmatrix} F_x \\ F_y \\ F_z \end{Bmatrix}_{ext} = m \left( \begin{Bmatrix} \dot{u} \\ \dot{v} \\ \dot{w} \end{Bmatrix} + [\omega] \begin{Bmatrix} u \\ v \\ w \end{Bmatrix} \right) \quad (2.30)$$

$$\Sigma \begin{Bmatrix} M_x \\ M_y \\ M_z \end{Bmatrix}_{ext} = [J] \begin{Bmatrix} \dot{p} \\ \dot{q} \\ \dot{r} \end{Bmatrix} + [\omega][J] \begin{Bmatrix} p \\ q \\ r \end{Bmatrix} \quad (2.31)$$

Where  $\{F_*\}_{ext}$  and  $\{M_*\}_{ext}$  are the external forces and moments on the body,  $m$  is the total mass of the system, thus payload mass plus parafoil mass, and  $[J]$  is the inertial tensor defined as:

$$[J] = \begin{bmatrix} (j_{xx_p} + j_{xx_v}) + mZ_{cg}^2 & -(j_{xy_p} + j_{xy_v}) & -(j_{xz_p} + j_{xz_v}) \\ -(j_{xy_p} + j_{xy_v}) & (j_{yy_p} + j_{yy_v}) + mZ_{cg}^2 & -(j_{yz_p} + j_{yz_v}) \\ -(j_{xz_p} + j_{xz_v}) & -(j_{yz_p} + j_{yz_v}) & (j_{zz_p} + j_{zz_v}) \end{bmatrix} \quad (2.32)$$

$Z_{cg}$  is represented in Figure 2.14, the parameters  $j$  with index  $p$  are the moments of inertia of the parafoil, while the ones with index  $v$  are the moments of inertia of

the payload.

The external forces and moments have three main contributions expressed in body frame: weight force and the weight induced moments ( $F_g, M_g$ ), aerodynamic forces and moments ( $F_{aero}, M_{aero}$ ) and the apparent mass contributions ( $F_{app}, M_{app}$ ).

$$\begin{aligned} \Sigma \begin{Bmatrix} F_x \\ F_y \\ F_z \end{Bmatrix}_{ext} &= F_{aero} + F_{app} + F_g \\ \Sigma \begin{Bmatrix} M_x \\ M_y \\ M_z \end{Bmatrix}_{ext} &= M_{aero} + M_{app} + M_g \end{aligned} \tag{2.33}$$

### Weight force and moments

The weight force and the weight induced moments are so expressed:

$$\begin{aligned} F_g &= m \cdot [R_I^B] \begin{Bmatrix} 0 \\ 0 \\ g \end{Bmatrix} \\ M_g &= \begin{bmatrix} -mgZ_{cg} \sin \phi \cos \theta \\ -mgZ_{cg} \sin \theta \\ 0 \end{bmatrix} \end{aligned} \tag{2.34}$$

### Aerodynamic forces and moments

Both the parafoil and the payload give an aerodynamic contribution. Obviously the payload's contribution is lower, but not negligible. The aerodynamic forces and moments are described using a formulation based on aerodynamic derivatives [2],

which can be non-linear, but with a 6 DoF model they can be considered steady.

$$\begin{aligned}
 F_{\text{aero}} &= F_{\text{aero parafoil}} + F_{\text{aero vehicle}} \\
 F_{\text{aero parafoil}} &= L_p \begin{bmatrix} \sin(\alpha + \tau) \\ 0 \\ -\cos(\alpha + \tau) \end{bmatrix} - D_p \begin{bmatrix} \cos(\alpha + \tau) \\ 0 \\ -\sin(\alpha + \tau) \end{bmatrix} + \begin{bmatrix} 0 \\ Y_p \\ 0 \end{bmatrix} \\
 L_p &= \frac{1}{2}\rho V_T^2 S C_L \\
 D_p &= \frac{1}{2}\rho V_T^2 S C_D \\
 Y_p &= \frac{1}{2}\rho V_T^2 S C_Y \\
 F_{\text{aero vehicle}} &= \frac{1}{2}\rho V_T^2 \begin{bmatrix} S C_x \\ S C_y \\ S C_z \end{bmatrix}
 \end{aligned} \tag{2.35}$$

$$\begin{aligned}
 M_{\text{aero}} &= M_{\text{aero parafoil}} + M_{\text{aero vehicle}} \\
 M_{\text{aero parafoil}} &= \frac{1}{2}\rho V_T^2 S \begin{bmatrix} b C_l \\ c C_m \\ b C_n \end{bmatrix} \\
 M_{\text{aero vehicle}} &= \frac{1}{2}\rho V_T^2 S_v \begin{bmatrix} d C_l \\ d C_m \\ d C_n \end{bmatrix}
 \end{aligned} \tag{2.36}$$

In these formulas  $V_T$  is the *free stream velocity*, which is seen by the parafoil with an inclination of  $\alpha$  (angle of attack) plus  $\tau$  (rigging angle of the parafoil).  $S_v$  and  $d$  are the payload reference area and reference length;  $S$ ,  $b$  and  $c$  are the parafoil's wing area, wing span and wing chord.

All the moments and forces are dependent from aerodynamic coefficients, which depend from the geometry and aerodynamic features of the parafoil and they are composed of both stability and control derivatives. For a rectangular straight wing the coefficients can be written as:

- *Longitudinal dynamics parafoil's coefficients*

$$\begin{aligned}
 C_L &= C_{L,0} + C_{L,\alpha}\alpha \\
 C_D &= C_{D,0} + \frac{C_L^2}{\pi e AR} \\
 C_m &= C_{m,0} + C_{m,\alpha}\alpha + \frac{c\cdot q}{2V_T}C_{m,q}
 \end{aligned} \tag{2.37}$$

where  $AR = b/c$  is the aspect ratio of the wing and  $e$  is the Oswald's factor.

- *Lateral-directional parafoil's coefficients*

$$\begin{aligned}
 C_Y &= C_{Y,\beta}\beta + C_{Y,\delta}\delta_a \\
 C_l &= C_{l,\beta}\beta + C_{l,\delta_a}\delta_a + \frac{b\cdot p}{2V_T}C_{l,p} + \frac{b\cdot r}{2V_T}C_{l,r} \\
 C_n &= C_{n,\beta}\beta + C_{n,\delta_a}\delta_a + \frac{b\cdot p}{2V_T}C_{n,p} + \frac{b\cdot r}{2V_T}C_{n,r}
 \end{aligned} \tag{2.38}$$

where  $\beta$  is the sideslip angle, while  $\delta_a$  is the deflection angle of the control surfaces.

The aerodynamic derivatives are difficult to estimate without wind tunnel tests or CFD simulations. Since this is a preliminary study it has been decided to use values of a similar existing parafoil, which are presented in the 3rd Chapter. Furthermore a ram-air parachute is not a straight wing, but as an arc shape, thus this geometry as an effect on the aerodynamic, in particular on the *longitudinal dynamics coefficients*. These aspects have been taken into account in the design of the parafoil system and are well discussed in the 3rd Chapter.

### Apparent mass effect

A ram-air parachute's structure is very light, which means that it is heavily influenced by the air passing over and around it. The pendulum motion of a parafoil system is affected since the point of rotation moves away from the CG of the system and towards the parafoil [5]. Usually for conventional aircraft this effect is negligible, but since the volume of air captured inside the parafoil is high, the moment of inertia and the inertia of the system increase considerably. The

apparent mass effect can be computed with the simplified formulations in Ref.[18]:

$$\begin{aligned}
 [K_{\text{app}}] &= \begin{bmatrix} A & 0 & 0 \\ 0 & B & 0 \\ 0 & 0 & C \end{bmatrix} \\
 [I_{\text{app}}] &= \begin{bmatrix} I_A & 0 & 0 \\ 0 & I_B & 0 \\ 0 & 0 & I_C \end{bmatrix}
 \end{aligned} \tag{2.39}$$

$$F_{\text{app}} = -[K_{\text{app}}] \dot{V} - \omega \wedge ([K_{\text{app}}] V)$$

$$M_{\text{app}} = -[I_{\text{app}}] \dot{\omega} - \omega \wedge ([I_{\text{app}}] \omega) - V \wedge ([K_{\text{app}}] V)$$

$A$ ,  $B$ ,  $C$  and  $I_A$ ,  $I_B$ ,  $I_C$  are the volumes associated with the apparent masses and inertias for translation or rotation along each axis [18] represented in Figure 2.15 and calculated with the equations:

$$A = 0.666\rho \left(1 + \frac{8}{3}\bar{a}^2\right) t^2 b$$

$$B = 0.267\rho \left(1 + 2\frac{\bar{a}^2}{t^2} AR \left(1 - \bar{t}^2\right)\right) t^2 c \tag{2.40}$$

$$C = 0.785\rho \sqrt{1 + 2\bar{a}^2 \left(1 - \bar{t}^2\right) \frac{AR}{1+AR}} c^2 b$$

$$I_a = 0.055\rho \frac{AR}{1+AR} c^2 b^3$$

$$I_b = 0.0308\rho \frac{AR}{1+AR} \left[1 + \frac{\pi}{6}(1 + AR) AR \bar{a}^2 \bar{t}^2\right] c^4 b \tag{2.41}$$

$$I_c = 0.0555\rho \left(1 + 8\bar{a}^2\right) t^2 b^3$$

$$AR = \frac{b}{c} \quad \bar{t} = \frac{t}{c} \quad \bar{a} = \frac{a}{b} \tag{2.42}$$

Obviously, as it can be seen in the Equations 2.40 and 2.41, the apparent masses and inertias are dependent from the atmospheric density  $\rho$ . On Mars  $\rho$  is nearly 100 times lower than on Earth, for this reason the contribution of the apparent mass effect is negligible, as shown in the table below. Therefore the parafoil's dynamics simulator, developed in this thesis, doesn't take into account it's contribution.

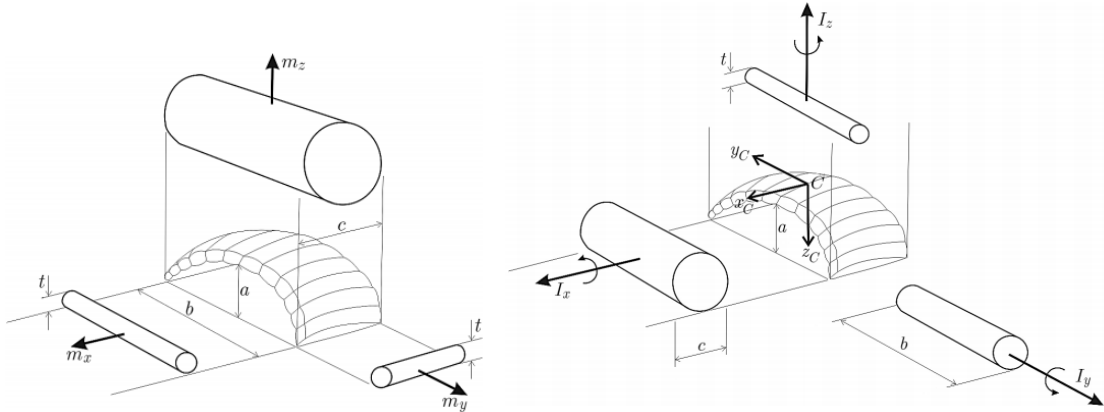


**Figure 2.15:** Volumetric Representation of Apparent Masses and Moments [18]

**Table 2.2:** apparent masses and inertias comparison between Earth and Mars for a parafoil of 13 m<sup>2</sup> wing surface

	<b>Earth</b>	<b>Mars</b>
$\rho$ kg/m <sup>3</sup>	1.225	0.015
$A$ kg	2.322	0.028
$B$ kg	1.136	0.014
$C$ kg	31.082	0.381
$I_A$ kg m <sup>2</sup>	53.333	0.654
$I_B$ kg m <sup>2</sup>	5.929	0.073
$I_C$ kg m <sup>2</sup>	18.915	0.232

## Chapter 3

# Parafoil's dynamics simulator

The purpose of this chapter is to illustrate the designing and modeling of the parafoil system and the overall structure of the dynamics simulator developed on MATLAB-Simulink. The simulator is composed by two parts: a pre-processing block which provides the design process, and a Simulink model which simulates the behavior of the system in the martian environment in different conditions. The first part, that can be called design block, is composed by many subroutines, which defines the geometric and aerodynamic features of the parafoil, while the Simulink model, taking the needed parameters from the first block, show the trend of the variables of the system and its motion over the simulation set time. The overall scheme work of the simulator can be described by the flow chart reported in Figure 3.1, which illustrates the following steps:

1. geometric and aerodynamic inputs are initialized in the *main* subroutine and a value of the wing area is assumed,
2. with the inputs present in the *main* another subroutine calculates the aerodynamic coefficients of the parafoil;
3. the mass of the canopy and suspension lines are calculated. Moreover the dimensions of the parafoil, like  $b$ ,  $c$ ,  $\beta$ , etc., are defined.
4. knowing the total mass and the wing area, the wing loading is defined.
5. the design point of  $C_L = 0.5$  is imposed. If the velocity constrains are satisfied the cycle stops; if they aren't a bigger wing area is assumed and the cycle restarts.
6. the results are saved in the *main* subroutine;

7. the rigging angle and the CoM position are defined, then another subroutine is called to calculate the inertia tensor. All the results are saved in the *main*;
8. the initial conditions of the system and the landing point are defined in the *main*;
9. the Simulink model is executed taking all the constants from the *main* subroutine and giving in output the variables evolution over the set time.

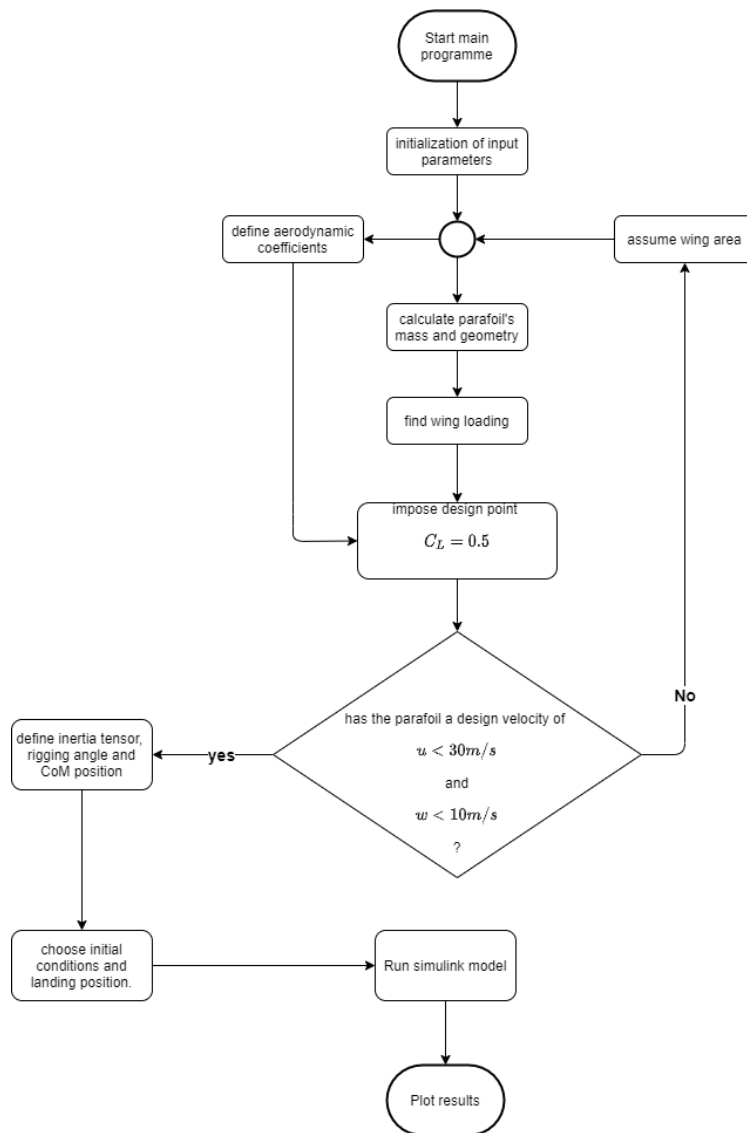


Figure 3.1: Parafoil system simulator flow chart

In the following sections all the formulations and parameters used for the design block, as well as the results of the designing process are presented. Moreover the structure of the Simulink model is discussed, with a focus on the architecture of the GNC system.

### 3.1 The rover

The main input parameter to design the parafoil is the payload that has to bring. For this study the chosen payload is the JPL open source rover, which is a scaled down version of the 6 wheel rover design that JPL uses to explore the surface of Mars. The Open Source Rover is designed almost entirely out of Consumer Off The Shelf (COTS) parts [19]. In the table below the rover's characteristics are shown.

**Table 3.1:** Rover's characteristics

Attribute	Value [imperial]	Value [SI]
Weight	28 [lbs]	12.7 [kg]
Footprint	24x14 [in]	60.96x30.48 [cm]
Battery Capacity	5200 [mAh]	5200 [mAh]
Battery Discharge Rate	8 [A]	8 [A]
Nominal Current Draw	1.2 [A]	1.2 [A]
Operating time	5 [hrs] (continual use)	5 [hrs] (continual use)
Approximate Max speed	68.8 [in/s]	1.75 [m/s]
Maximum 90 deg vertical scale	12 [in]	30.48 [cm]
Maximum height differential between sides	14 [in]	35.56 [cm]

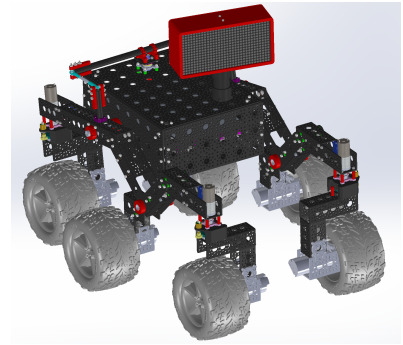


**Figure 3.2:** JPL's open source rover

The design of the parafoil is based on the weight of the rover reported on the Table 3.1. Moreover to estimate the aerodynamic drag of the payload, it has been considered in a compact configuration, therefore with all the legs retracted. In this configuration the rover is similar to a rectangular of  $55\text{cm} \times 55\text{cm} \times 20\text{cm}$ .

### 3.2 Parafoil's design

The design of the parafoil system is based on the method presented in Ref. [5] and [17]. Where a lifting line theory for low aspect wings is used to estimate the lift and drag coefficients, the longitudinal stability and flight performance. Knowing these factors it can be easily estimated the needed wing area.

A parafoil can be considered as a ram-air wing attached to the payload with long suspension lines, which give an arc-anhedral angle to the wing. The amount of arc

anhedral is a function of the ratio of line length ( $R$ ) to span ( $b$ ) [17]. The wing alone performance improves with increasing aspect ratio but, for a given value of  $R/b$ , the larger the aspect ratio the greater the line length. In addition, the number of lines tends to increase with aspect ratio. Thus increasing aspect ratio gives markedly higher line drag. Reducing  $R/b$ , for a given aspect ratio reduces line drag but yields an increasingly inefficient wing [17]. Moreover the shape of the wing can increase the efficiency of the parafoil, but for simplicity a rectangular wing shape has been chosen. To obtain a good gliding ratio, the following parameters were selected:

**Table 3.2:** Parafoil's parameters

<i>Parafoil's parameters</i>	
$AR$	3
$R/b$	0.8
lines diameters	25 mm
number of lines	1 for 1.11 $m^2$ of wing area

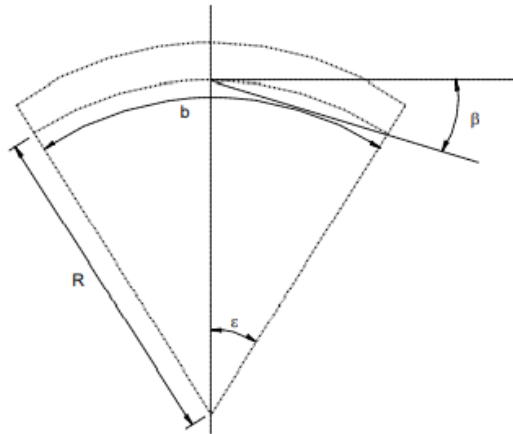


**Figure 3.3:** Definition of anhedral angle for a ram-air wing [17]

Another important input parameter is the airfoil shape, which has major effects on the overall aerodynamic efficiency of the parafoil. For this study a CLARK-Y 18% airfoil has been chosen. In Figure 3.4 the theoretical lift curve is presented. The value of slope  $a_0$  is  $6.89 \text{ rad}^{-1}$  and the  $\alpha_{zl}$  is equal to  $-7^\circ$ . Furthermore, the airfoil of a ram-air parachute has an opening on the nose of the profile to let in the air, which inflate the wing. This opening has an influence on the total drag, the bigger it is the more increase the drag, but a too small opening would be unable to inflate efficiently the parafoil. For this study an open airfoil nose of  $h = 0.08c$ , where  $c$  is the chord of the parafoil, has been selected. Based on these

input parameters it's possible to estimate the aerodynamic features and dimensions of the parafoil.

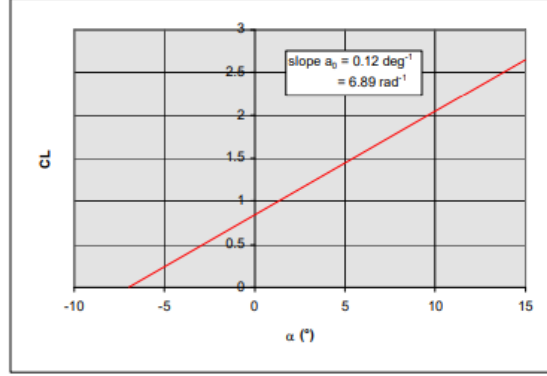


**Figure 3.4:** Theoretical section lift coefficient for an 18% Clark Y ram-air parachute airfoil [17]

### 3.2.1 Aerodynamic features

Once inflated a ram-air parachute is essentially a low aspect wing and thus conventional wing theory is applicable [17]. For this reason the lift curve slope  $a$  can be estimated with the lifting line theory, taking into account the low aspect ratio of ram-air parachutes, which is usually lower than 5. Introducing a corrective parameter  $k$  in the lifting line formula, it can be obtained a good approximation of  $a$  as reported in Ref. [20].

$$a = C_{L\alpha} \approx \frac{AR\pi}{\sqrt{k^2+1}+1} \quad (3.1)$$

$$k = \frac{AR\pi}{a_0}$$

Therefore it's possible to estimate the lift curve slope of the entire wing, knowing the lift curve slope of the airfoil ( $a_0$ ) and the aspect ratio. If the wing has an  $AR < 2.5$  a non-linear component of  $C_L$ , caused by the drag based on the normal velocity component [17] must be taken into account. For a high aspect wing this contribution is negligible because the wing span is high and the surface affected by the normal velocity is a small part of the entire wing; while for a low aspect wing this region is a good portion of the overall wing surface. The  $C_L$  equation can so be written as:

$$\begin{cases} C_L = a(\alpha - \alpha_{ZL}) + k_1 \sin^2(\alpha - \alpha_{ZL}) \cos(\alpha - \alpha_{ZL}) & \text{for } AR < 2.5 \\ C_L = a(\alpha - \alpha_{ZL}) & \text{for } AR > 2.5 \end{cases} \quad (3.2)$$

Where  $k_1 = 3.33 - 1.33AR$ .

For this study, as reported before, a ram-air wing with  $AR = 3$  has been chosen, thus the non-linear component can be neglected. Comparing the analytical formula with the experimental data of NASA and the University of Notre Dame, shown in Figure 3.5, it can be seen that the match is acceptable up to the stall. Both sets of experimental data show that ram-air canopies stall at lower angles of incidence than rigid wings of corresponding section and aspect ratio. Ware and Hassell and Ross propose that the reason for this early stall is that the sharp leading edge of the upper lip of the open nose causes leading edge separation at relatively low lift coefficients [17]. Also can be noticed that for NASA's data stall occurs at  $C_L \approx 0.7$ , while for Notre Dame at  $C_L \approx 0.85$ . The reason of this disparity, could depend on the models used: NASA used flexible models, while the University of Notre Dame used semi-rigid models.

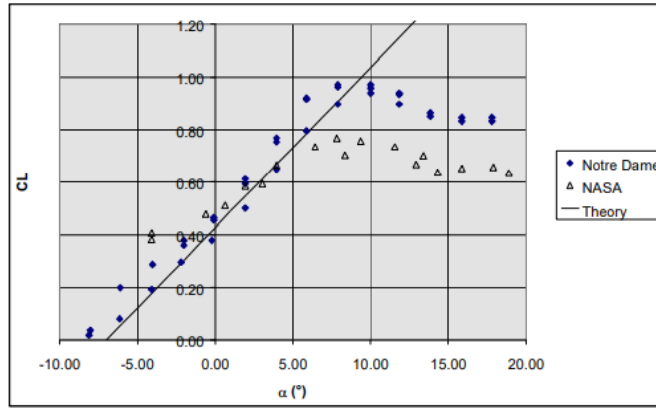


**Figure 3.5:** Experimental and theoretical lift coefficients for a ram-air wing [17],  $AR = 3.0$

The parafoil is not a straight ram-air wing, but has an arc-anhedral angle ( $\beta$ ) due to the suspension lines. The  $C_L$  is affected by this angle in the following way:

$$C_L = C_{L\beta=0} \cos^2 \beta \quad (3.3)$$

$$\beta = \varepsilon/2 \quad (3.4)$$

$$\varepsilon = b/2R$$

A similar discussion can be made for the drag coefficient, which can be expressed

as:

$$\begin{cases} C_D = C_{D0} + \frac{C_{Lc}^2 (1+\delta)}{\pi AR} + k_1 \sin^3(\alpha - \alpha_{ZL}) & \text{for } AR < 2.5 \\ C_D = C_{D0} + \frac{C_{Lc}^2 (1+\delta)}{\pi AR} & \text{for } AR > 2.5 \end{cases} \quad (3.5)$$

Where  $C_{Lc} = a(\alpha - \alpha_{zl})$  and  $1/(1 + \delta)$  is Oswald's factor.  $\delta$  is a corrective parameter for non-elliptical wing loading and increases with the aspect ratio of the wing, as reported in the plot below.

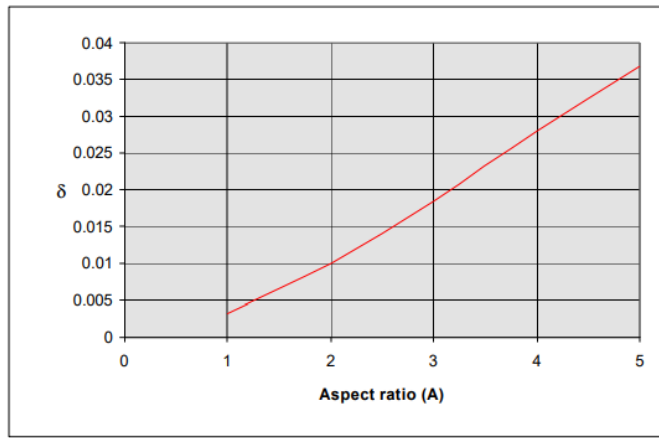


**Figure 3.6:**  $\delta$  for rectangular planform wings versus aspect ratio [17]

$C_{D0}$  is a sum of different drag contributions here reported:

- basic airfoil drag - for an airfoil of typical section -  $C_D = 0.015$ ;
- surface irregularities and fabric roughness -  $C_D = 0.004$ ;
- open airfoil nose -  $C_D = 0.5h/c$ ;
- drag of pennants and stabiliser panels - for pennants and stabilisers which do not flap -  $C_D = 0.0001$ .

This formulation is valid for a ram-air wing and agrees with experimental data of NASA and Notre Dame as shown in Figure 3.7.

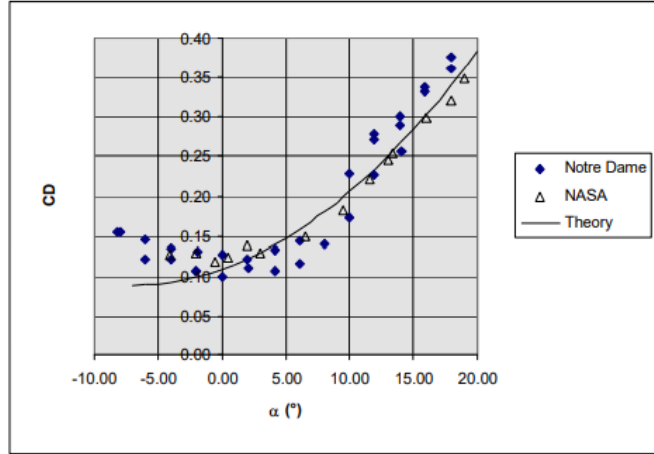


**Figure 3.7:** Experimental and theoretical drag coefficient for a ram-air wing [17],  $AR = 3.0$

Not only the ram-air wing give a drag contribution, also the payload and suspension lines. To simplify the estimation of line drag it is assumed that all lines are the same length and are subject to the same normal velocity  $V \cdot \cos \alpha$  where  $V$  is the system velocity. For typical Reynolds numbers the drag coefficient of a suspension line would be approximately 1.0. The contribution of line drag to the total system drag may therefore be estimated from [17]

$$C_{Dl} = \frac{nRd \cos^3 \alpha}{S} \quad (3.6)$$

where  $n$  is the number of lines,  $R$  mean line length,  $d$  the line diameter and  $S$  the canopy area. While the payload contribution may be written as

$$C_{Dv} = \frac{(C_D S)_v}{S} \quad (3.7)$$

where the numerator is the drag coefficient of the rover multiplied for its reference surface. The rover can be considered as a cuboid, thus it has a  $C_D = 1.05$ . The total drag coefficient of a parafoil system with  $AR = 3$  can be estimated with the following equation:

$$C_D = C_{D0} + C_{Dl} + C_{Dv} + \frac{C_{Lc}^2 (1 + \delta)}{\pi AR} \quad (3.8)$$

With Eq. 3.3 and 3.8 it is possible to estimate the Lift, Drag and the efficiency  $L/D$  of the parafoil system for every angle of attack. These information are sufficient to estimate the needed canopy area and geometric features of the parafoil, which are discussed in the section 3.2.2.

Typically the maximum theoretical value of lift to drag ratio occurs close to or beyond the stall for a conventional ram-air parachute. The maximum L/D is therefore not a useful measure to use for the performance of a ram-air parachute since, the wing cannot operate effectively close to the stall. Current ram-air parachutes are generally rigged to fly with a lift coefficient of around 0.5 [17]. Rigging the canopy means positioning the CG of the system such that the equilibrium attitude is at the required angle of attack. This equilibrium occurs when the sum of moments acting on the system is zero and when the slope of the pitching moment curve,  $dC_M/d\alpha$ , is negative [17]. Assuming that the system is rigid and that CoM of the canopy is positioned in the quarter chord point, the total moment  $M$  of the system may be written with reference to Figure 3.8:

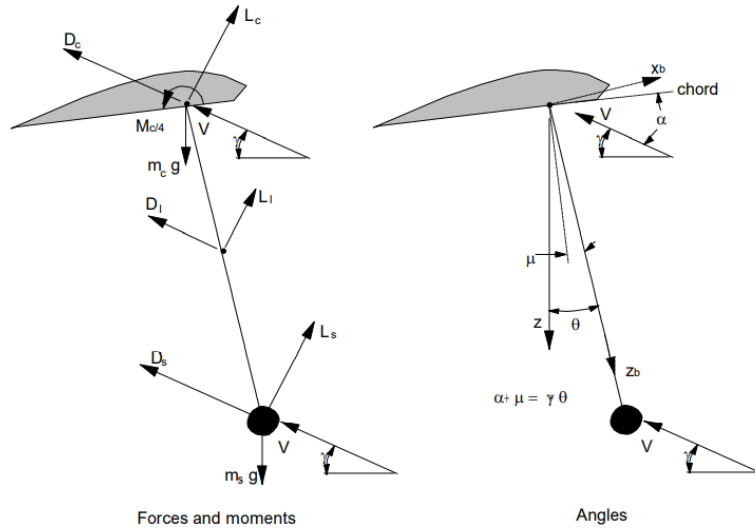


Figure 3.8: Definitions for static stability analysis [17]

$$M = M_{c/4} + R [L_v \sin(\alpha + \mu) - D_v \cos(\alpha + \mu)] + \frac{R}{2} [L_l \sin(\alpha + \mu) - D_l \cos(\alpha + \mu)] - m_v g R \sin \theta \quad (3.9)$$

where  $M_{c/4}$  is pitching moment of the canopy about 25% chord point, which is about -0.07 for a CLARK-Y airfoil,  $L_l$  is the lift force acting on the suspension lines,  $L_v$  is the lift force acting on the payload,  $D_l$  is the drag force acting on the suspension lines,  $D_v$  is the drag of the payload,  $m_v$  is the payload mass and  $\mu$  is the rigging angle. Line force is assumed acting normal to and at the mid-point of the line joining the 25% chord point to the payload. Therefore line drag and lift

may be written [17]:

$$C_{Di} = \frac{ndR \cos^3(\alpha + \mu)}{S} \tag{3.10}$$

$$C_{Li} = -\frac{ndR \cos^2(\alpha + \mu) \sin(\alpha + \mu)}{S}$$

Writing Eq. 3.9 in coefficient form, considering  $C_{Lv} = 0$  and substituting  $C_{Di}$  and  $C_{Li}$ :

$$C_M = C_{Mc/4} + \frac{R}{c} [-C_{Dv} \cos(\alpha + \mu)] - \frac{R}{2c} \frac{nRd \cos^2(\alpha + \mu)}{S} - \frac{m_v g R \sin \theta}{1/2 \rho V^2 S c} \tag{3.11}$$

Setting  $C_M = 0$  it's possible to find the value of the rigging angle  $\mu$ .  
Trough these calculations the following values were found for the parafoil system:

**Table 3.3:** Longitudinal dynamics

<i>Longitudinal Dynamics</i>	
$C_{L0}$	0.4066
$C_{L\alpha}$	3.1672
$C_{D0}$	0.0788
$C_{Mc/4}$	-0.0700
$\mu$	0.0241 rad

So far only the longitudinal dynamics has been discussed, but to control the parafoil also the lateral-directional dynamics must be taken into account, which are more complicated than the longitudinal dynamics since the roll and yaw terms are coupled [5] as it can be seen in Eq. 2.38. Lateral-directional terms, are complicated to estimate without flight testing. A method to estimate them analytically is presented in Ref. [20], but the results aren't reliable for a martian parafoil. Therefore it has been chosen to use the lateral-directional derivatives of a large parafoil presented in Ref. [5].

**Table 3.4:** Lateral-Directional Derivatives

<i>Lateral-directional derivatives</i>	
$C_{y,\beta}$	-0.24
$C_{l,\beta}$	-0.04
$C_{l,p}$	-4.5
$C_{l,r}$	0.8
$C_{n,\beta}$	0.16
$C_{n,p}$	0.8
$C_{n,r}$	-0.16

Moreover the control of the parafoil comes from the symmetric or asymmetric deflection of the outer trailing edges. Symmetric deflection affects the longitudinal dynamics and the gliding ratio, while the asymmetric deflection creates a difference of drag between the two sides, thus a yawing moment. The control deflections are so expressed:

$$\begin{aligned}\delta_a &= \delta_r - \delta_l \\ \delta_s &= \frac{\delta_r + \delta_l}{2}\end{aligned}\tag{3.12}$$

Where  $\delta_r$  and  $\delta_l$  are the right and left edge deflections,  $\delta_s$  is the symmetric control deflection, while  $\delta_a$  is the asymmetric one. Since the control surfaces have an influence also in the longitudinal dynamics, in particular on the  $C_L$  and  $C_D$ , the Eq. 3.3 and 3.8 become:

$$\begin{aligned}C_L &= \{a(\alpha - \alpha_{zl})\} \cos^2 \beta + C_{L,\delta} (2\delta_s + |\delta_a|) \\ C_D &= C_{D_0} + \frac{C_L^2}{\pi AR} (1 + \delta) + C_{Dl} + C_{Dv} + C_{D,\delta} (2\delta_s + |\delta_a|)\end{aligned}\tag{3.13}$$

Likewise the lateral-directional derivatives, also the control derivatives were taken from Ref. [5] and are shown in the following table:

**Table 3.5:** Control Derivatives

<i>control derivatives</i>	
$C_{y,\delta a}$	-0.0096
$C_{l,\delta a}$	-0.252
$C_{n,\delta a}$	-0.04
$C_{L,\delta s}$	0.13
$C_{D,\delta s}$	0.08

The  $C_M$  is not affected by control derivatives, but from the pitching velocity  $q$ . His effect is described by the damping derivative  $C_{M,q}$ . The value of the derivative has been taken from Ref. [5]. Taking into account this contribution we have:

$$C_M = C_{MC/4} + \frac{R}{c} [-C_{Dv} \cos(\alpha + \mu)] - \frac{R}{2c} \frac{nRd \cos^2(\alpha + \mu)}{S} + C_{M,q} \frac{qc}{2V_T} \quad (3.14)$$

Where  $C_{M,q} = -6.1$ .

With the formulations discussed in this section the overall aerodynamic features of the parafoil are defined, but as shown in Eq. 2.35 and 2.36 also the payload give a contribution to the aerodynamic total forces and moments, but is small compared to the parafoil. Thus, for simplicity the only payload's aerodynamic contribution considered in this study is the drag force in  $x_b$  direction, all the other aerodynamic forces and moment are neglected. Therefore the formulations presented in this section describe the aerodynamic features of the overall system and not only of the parafoil.

Knowing the aerodynamic characteristics of the system, it's possible to size the parafoil to sustain the payload and to have a low descent velocity. The designing method is discussed in the following section.

### 3.2.2 Parafoil's dimensions

The geometric features required to define the parafoil system are: the total mass of the system  $m$ , the canopy surface  $S$ , the tensor of inertia  $J$  and the position of the CoM of the system  $Z_{cg}$ .

Once the value of  $S$  is known, with the input parameters discussed above it's possible to evaluate  $b$ ,  $c$ ,  $R$ , number of lines ( $n$ ),  $\epsilon$  and  $\beta$ . Moreover, knowing the materials of the lines and the canopy, it's possible to evaluate the parafoil

system total mass, since the rover's mass is given. For this study the typical materials of canopies and suspension lines have been considered: nylon for the canopy ( $\rho_p = 44g/m^2$ ) and unsheathed Aramide/Kevlar for the suspension lines ( $\rho_l = 1.15kg/dm^3$ ).

To find the needed  $S$  an iterative algorithm on MATLAB has been implemented. Starting from an initial value of  $S$ , after evaluating the canopy and suspension lines mass, the wing loading  $W/S$  is calculated:

$$\frac{W}{S} = \frac{g(m_v + m_p + m_l)}{S} = \frac{g m}{S} \quad (3.15)$$

Knowing  $W/S$ ,  $C_D$  and  $C_L$  the velocity can be written as:

$$V = \left( \frac{2W}{\rho S \sqrt{C_L^2 + C_D^2}} \right)^{\frac{1}{2}} \quad (3.16)$$

$$u = V \cos \gamma$$

$$w = V \sin \gamma$$

$$\gamma = \arctan \frac{1}{L/D} \quad (3.17)$$

Considering a design  $C_L = 0.5$  the iterations stop when  $S$  is large enough to sustain the payload with a descent velocity  $w < 10$  m/s and  $u < 30$  m/s, thus having a good gliding ratio and a not excessive landing velocity. Moreover, once the distance  $R$  and the masses  $m_p$  and  $m_v$  are known, the CoM position  $Z_{cg}$  can be found. Through this algorithm the following values have been defined:

**Table 3.6:** Parafoil's geometric features

<i>Parafoil's geometric features</i>	
$S$	14 m <sup>2</sup>
$b$	6.48 m
$c$	2.16 m
$R$	5.18 m
$n$	13
$\epsilon$	0.625 rad
$\beta$	0.3125 rad
$m_p + m_l$	0.985 kg
$Z_{cg}$	5.05 m

The last characteristic to be defined is the inertia tensor  $J$ . To evaluate it, the parafoil is assumed to be a parallelepiped of dimensions  $b_{\text{inflated}}$ ,  $c$  and  $h_{\text{mean}}$  like

in Ref. [21]. The  $h_{mean}$  is an ‘‘apparent thickness’’ that keeps into account the parafoil mean thickness and the parafoil chamber and  $b_{inflated}$  is the actual span when the parafoil is fully inflated. They are defined as:

$$\begin{aligned} h_{mean} &= \frac{v_{vol}}{c b_{inflated}} \\ b_{inflated} &= 2R \sin(\epsilon) \\ v_{vol} &= 0.09c^2b \end{aligned} \tag{3.18}$$

Where  $v_{vol}$  represent the air volume inside the canopy. Considering the canopy mass  $m_p$  and the inside air mass, the parafoil inertia becomes:

$$\begin{aligned} j_{xxp} &= \left( \frac{v_{vol}\rho+m_p}{12} \right) (b_{inflated}^2 + h_{mean}^2) \\ j_{yy p} &= \left( \frac{v_{vol}\rho+m_p}{12} \right) (c^2 + h_{mean}^2) \\ j_{zzp} &= \left( \frac{v_{vol}\rho+m_p}{12} \right) (b_{inflated}^2 + c^2) \end{aligned} \tag{3.19}$$

To estimate the total inertia tensor, also the inertia of the payload is needed. Considering it as a parallelepiped as well, with  $x_v = 0.55m$ ,  $y_v = 0.55m$  and  $z_v = 0.2m$ , the moments of inertia are defined as:

$$\begin{aligned} j_{xxv} &= \frac{m_v}{12} (y_v^2 + z_v^2) \\ j_{yyv} &= \frac{m_v}{12} (x_v^2 + z_v^2) \\ j_{zzv} &= \frac{m_v}{12} (x_v^2 + y_v^2) \end{aligned} \tag{3.20}$$

From these formulations the total inertia tensor can be estimated with the Eq. 2.32, but since the overall system has two planes of symmetry, the tensor is diagonal. In the Table 3.7 the total inertia values are reported.

$$[J] = \begin{bmatrix} J_{xx} & 0 & 0 \\ 0 & J_{yy} & 0 \\ 0 & 0 & J_{zz} \end{bmatrix} \tag{3.21}$$

**Table 3.7:** Total moment of inertia of the parafoil system

<i>Total moment of inertia</i>	
$J_{xx}$	353.76 kg m <sup>2</sup>
$J_{yy}$	351.02 kg m <sup>2</sup>
$J_{zz}$	4.18 kg m <sup>2</sup>

### 3.3 Simulator's structure

Once the parafoil system is fully defined through the designing process explained above, it's possible to develop a Simulink model of the system, shown in Figure 3.9 that describes the evolution over time of the dynamics model's variables. The model is structured in the following blocks:

1. **GNC:** the Guidance, Navigation and Control system block is formed by a guidance algorithm, which uses position, heading angle, yaw and roll rate of the parafoil to generate a command output  $\delta_a$ , which leads the parafoil to the chosen Landing Position. In the section 3.3.1 the structure of the GNC system is discussed.
2. **WIND MODEL:** this block is formed by the algorithm presented in section 2.5, but since the added velocity is in body frame, the wind module is multiplied to the rotational matrix  $[R_B^I]$ .
3. **MARS ENVIROMENT:** it contains the atmosphere model described in section 2.4.
4. **EXTERNAL FORCES and MOMENTS:** knowing  $\rho$ ,  $V_T$ , the system attitude and the command  $\delta_a$ , the moments and forces acting on the system are calculated through the formulations reported in section 2.7.2.
5. **NEWTON'S II LAW and EULER'S EQUATIONS:** these two blocks represent the dynamics of the parafoil system. Taking the external forces and moments as inputs, provide the velocity and angular velocity of the parafoil in body frame.
6. **NAVIGATION EQUATIONS and ANGULAR KINEMATICS EQUATIONS:** the last two blocks describe the kinematics of the system and rotate the velocities and angular velocities from body to inertial frame, which are the final outputs of the Simulink model.

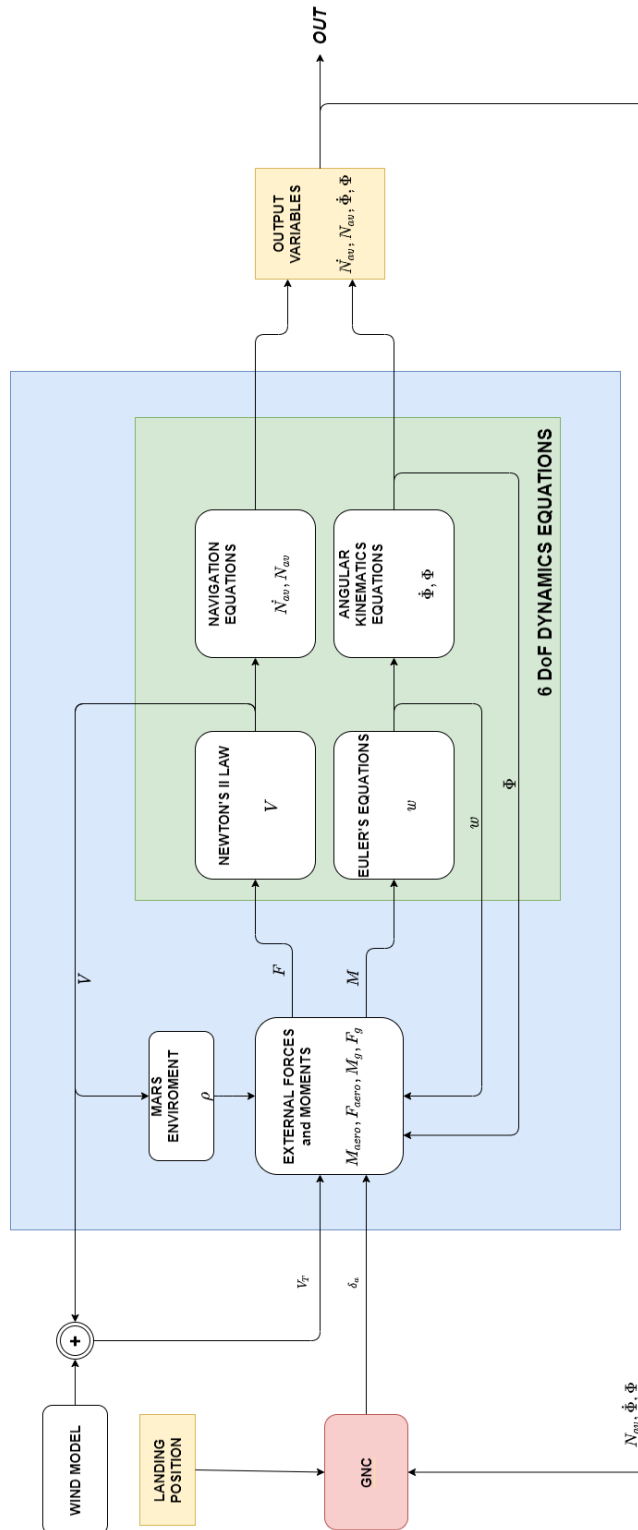
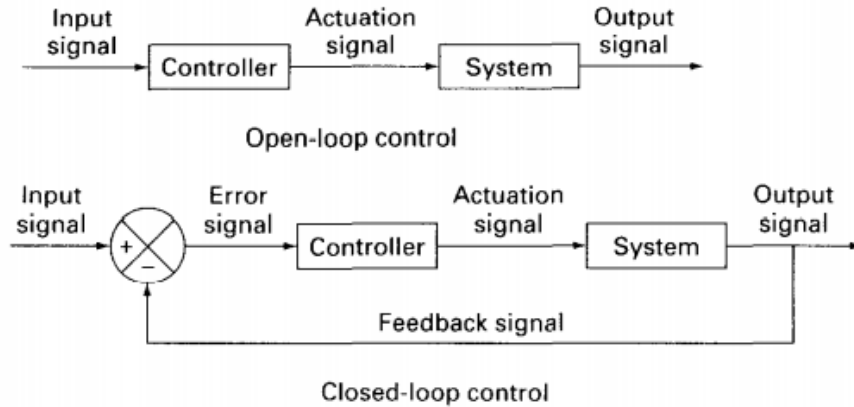


Figure 3.9: Parafoil system Simulink model

### 3.3.1 GNC

In this section the control law implemented for the parafoil system is presented. Control system can be classified in open-loop and closed loop systems, as presented in Figure 3.10. An open-loop control system is the simplest and least complex of all control devices. In the open-loop system the control action is independent of the output. In closed-loop system the control action depends on the output of the system. Closed-loop control systems are called feedback control systems. The advantage of the closed-loop system is its accuracy [22]. The feedback loops are used to compare the controlled signal with the command signal to generate an error signal. This error drives the output signal to overlap with the desired output.



**Figure 3.10:** Examples of open-loop and closed-loop control systems [22]

The control system chosen for the parafoil is based on the one presented in Ref. [5] and is a feedback control system composed by two cascade controllers: an outer loop and an inner loop. The first one is a position controller, which provides a command yaw rate proportional to the angle between the direction to the target and the vehicle's current heading vector [5]. The inner loop is an attitude controller and relies on the difference between the parafoil's current yaw rate and the command yaw rate coming from the up-stream controller, with an extra feedback given by the roll rate, which give more stability to the controller. Moreover inside the GNC block a switch from normal mode to spiral mode is present: when the distance error from the landing site is lower than a threshold radius, the algorithm switch to a constant deflection command  $\delta_a$ , that drives the system into a convergent spiral descent. This type of trajectory is safer than an altitude control during the whole descent phase aiming straight to the landing area. Circling always above the straight vertical path to the target means that if the gliding system exhibits a

sudden loss of altitude due to external factors (i.e. a significant change in wind intensity), it is still possible to reach the destination [2]. For simplicity the control of the parafoil is made only with the asymmetric deflection of the trailing edges  $\delta_a$ , the symmetric control  $\delta_s$  has not been taken into account. The overall structure of the GNC is presented in Figure 3.11.

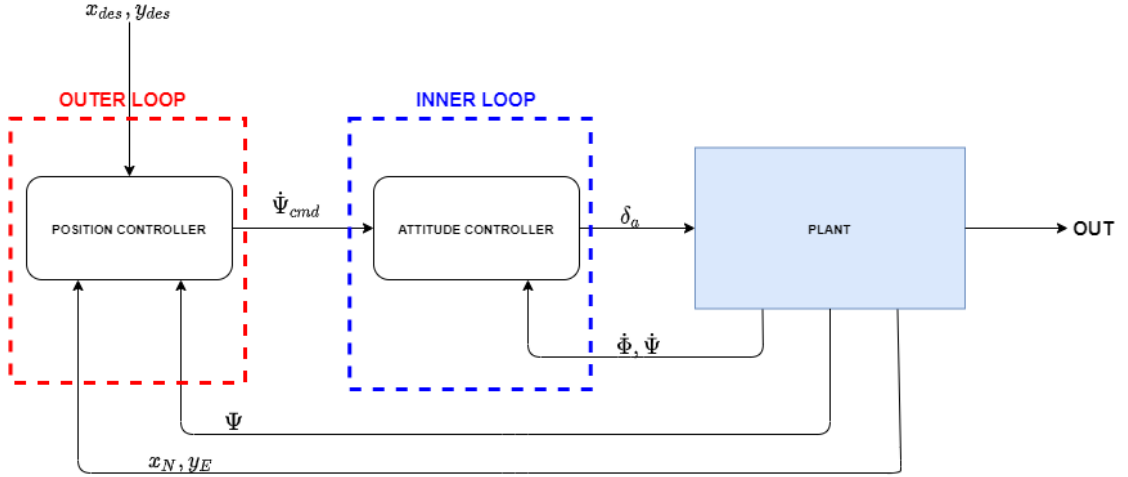


Figure 3.11: Overall GNC architecture

- **Position controller:** the first controller is based on a simple guidance law which attempts to move the vehicle's nose towards the landing point. The equations that governs this controller is:

$$\dot{\Psi}_{Cmd} = K \cdot \Delta\Psi = K (\Psi - \Psi_{Cmd}) \quad (3.22)$$

Where the  $\Psi_{Cmd}$  is defined as:

$$\Psi_{Cmd} = \arctan \frac{y_{des} - y_E}{x_{des} - x_N} \quad (3.23)$$

$\Delta\Psi$  is the angle between the direction to the target and the vehicle's current heading vector. A positive  $\Delta\Psi$  means the target is on the vehicle's right side, while a negative value for  $\Delta\Psi$  produces a left turn command. The gain value,  $K$ , reflects the responsiveness of the guidance law. Higher  $K$  values produce larger turn rate commands but may lead to instability [5], therefore saturation limits have been implemented on the output command.

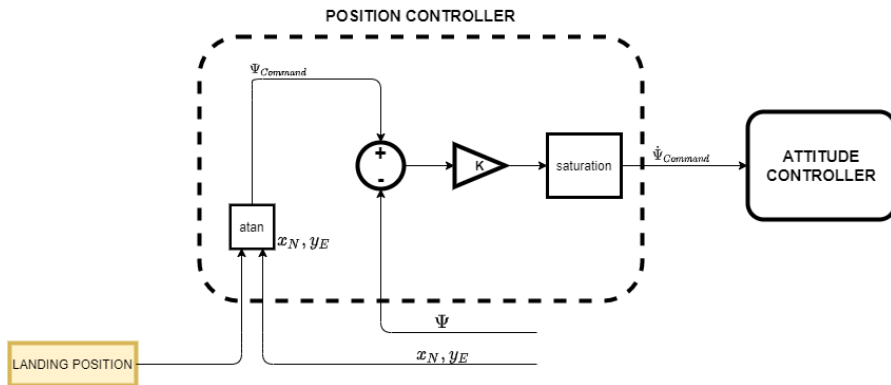


Figure 3.12: Position controller

- Attitude controller:** in the inner loop both roll and yaw rates are feedback to determine the asymmetric flap deflection needed to produce the desired turn rate. In this way stability problems are avoided. The attitude controller scheme is shown in Figure 3.13.

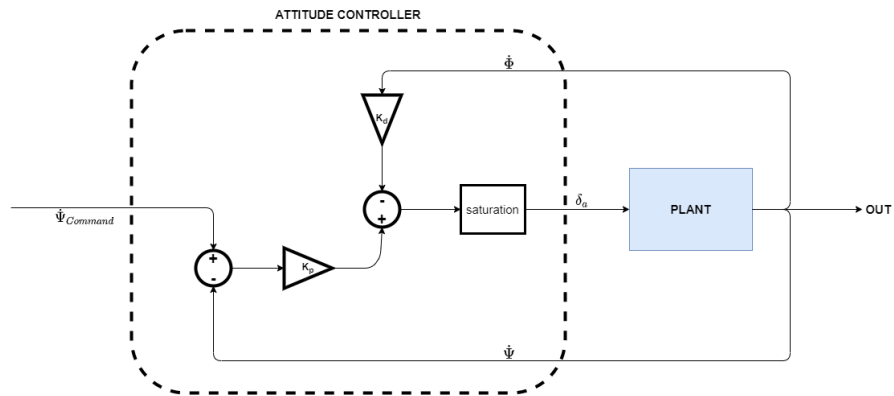


Figure 3.13: Attitude controller

In the table below, the controller parameters and the saturation at the output of the two controllers, determined by the trial and error tuning are reported.

**Table 3.8:** controllers parameters

<i>Position controller</i>		<i>Attitude controller</i>	
$K$	2	$K_p$	6
		$K_d$	10
$\dot{\Psi}_{cmd}$ saturation	$\pm\pi$ rad/s	$\delta_a$ saturation	$\pm 0.7$ rad

## Chapter 4

# Tests and results

Once the parafoil's dynamics simulator has been developed, before testing its behavior with the planned trajectory, the longitudinal stability of the system has been verified with a straight trajectory. As initial conditions  $-6000m$  of altitude and  $V_x = 10m/s$  has been chosen for all the simulations. The negative value of initial altitude is due to the reference frame, which has the  $z$  axis in Down direction. In Figure 4.1 it can be seen that, starting from the initial attitude of zero for every direction, after a transitory behavior,  $\theta$  settles near a value of  $-4.6^\circ$ , while the other angles remain equal to zero. Therefore the parafoil model is stable in the longitudinal flight.

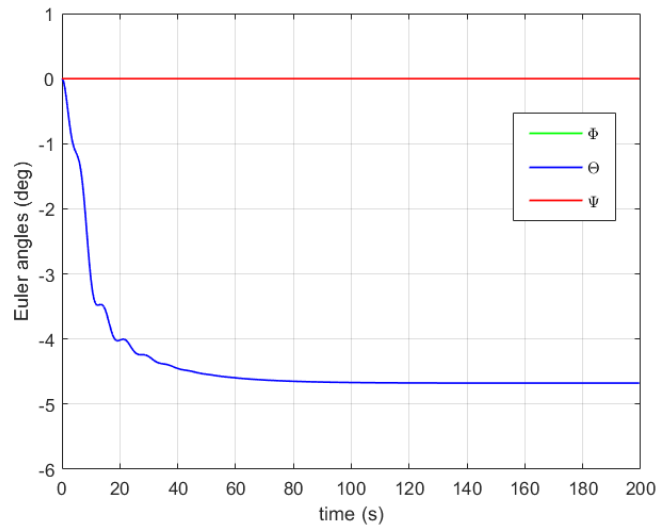


**Figure 4.1:** Parafoil's attitude

Moreover, it can be seen in Figure 4.2 that the velocity constraints imposed for the design of the canopy are fulfilled in the  $z_D$  direction, where  $V_z < 10m/s$  after a short transitory, while in  $x_N$  direction the limit of  $V_x < 30m/s$  is slightly exceeded. Although it can be noticed that leans toward the chosen value of  $V_x = 30m/s$ . With this velocities the system is able to perform a secure landing.

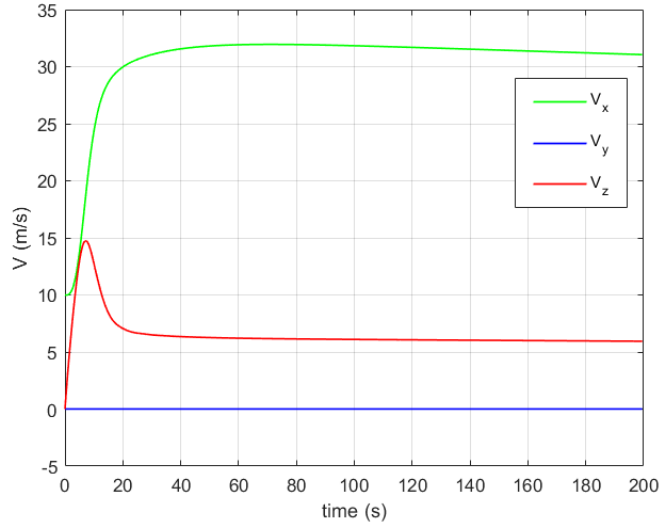


Figure 4.2: Parafoil's velocities

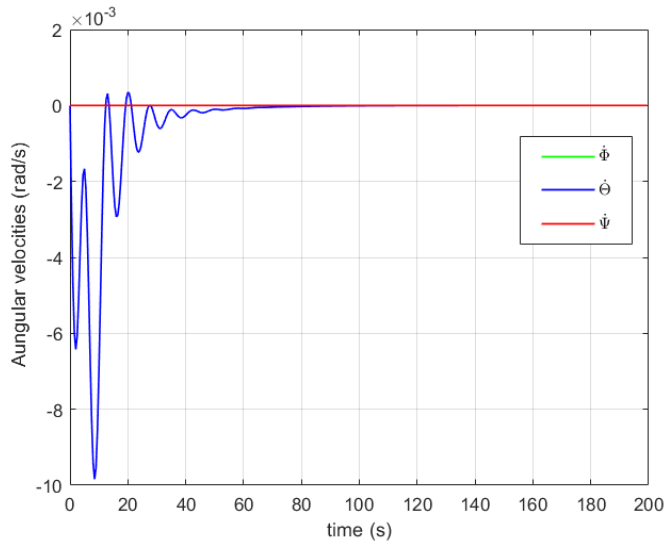
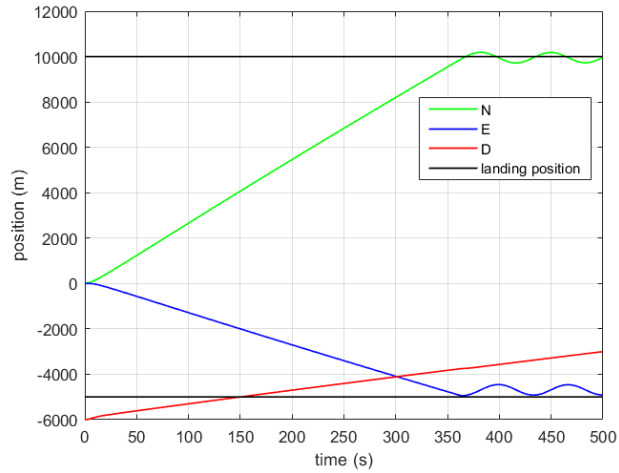


Figure 4.3: Parafoil's angular velocities

## 4.1 Trajectory

As said before, the chosen trajectory is a linear approach to the landing site with the highest gliding ratio, followed by a spiral descent above the landing area. In the figures 4.4, 4.5, 4.6 and 4.7 the trends of the system's variables for a landing  $10km$  North and  $-5km$  East are reported. The simulation time is higher than the one reported on figures, the trends after 500 s are the same as after 350 s simulation time, since at 350 s the parafoil start the spiral descent.



**Figure 4.4:** Parafoil's position

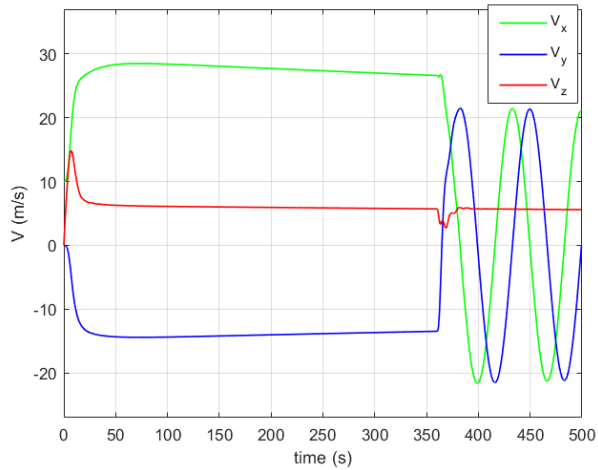


**Figure 4.5:** Parafoil's velocities

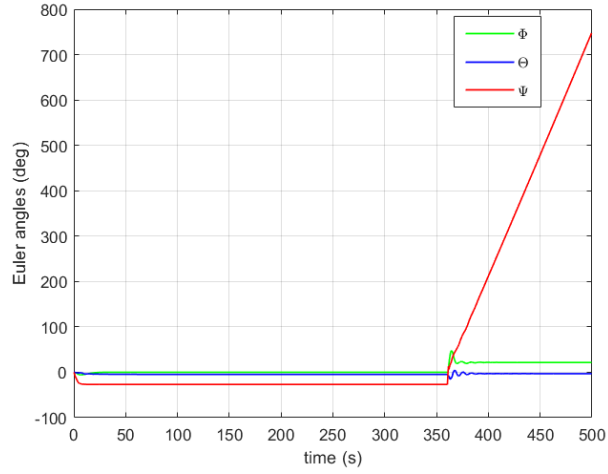


**Figure 4.6:** Parafoil's attitude

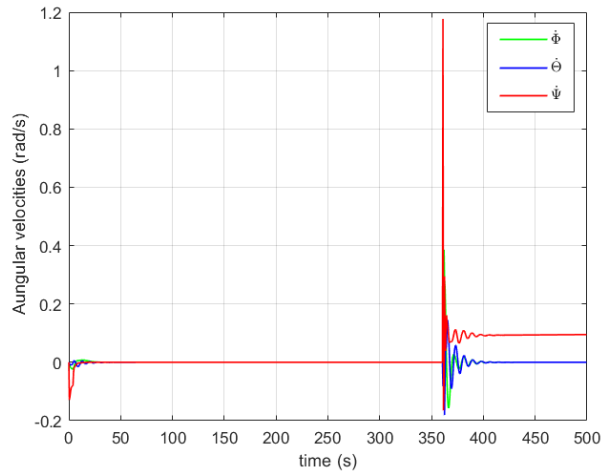


**Figure 4.7:** Parafoil's angular velocities

After an initial transitory where the heading vector of the parafoil turns towards the landing point, the variables of the system are steady. Also the lateral-directional dynamics is stable.

Once the parafoil is  $200m$  far from the landing point, the GNC switch to the spiral mode, where the command is maximum and blocked. With this type of algorithm the spiral descent is not perfectly upon the landing area, thus the parafoil lands far from the exact point. To solve this problem a MATLAB function has been implemented, which give as desired heading direction, not the exact landing point,

but a tangent line to the threshold circular area with  $radius = 200m$ . With this tangent trajectory the parafoil lands nearer to the landing point, as shown in Figures 4.8 and 4.9 .

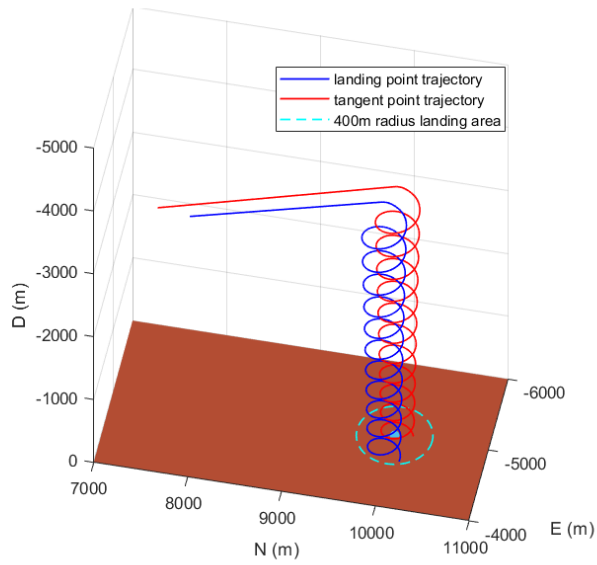


Figure 4.8: Comparison between two types of trajectories

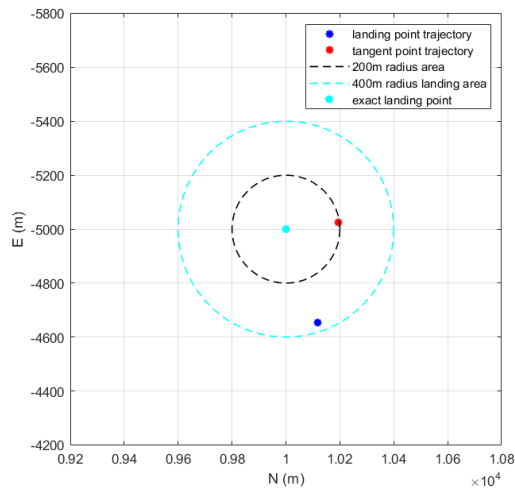


Figure 4.9: Comparison between two types of trajectories: upper view

Since the command is blocked during the final descent, it's difficult to land in the exact point, but with this tangent point trajectory the dispersion error is always lower than 400 m, while with the other trajectory the error was often higher. The chosen guidance law is quite reliable and allows to reach every desired point around the parafoil within 30 km. The GNC fail only when the  $\Delta\Psi = \pm\pi$ . In figures 4.10 and 4.11 some possible trajectories are shown.

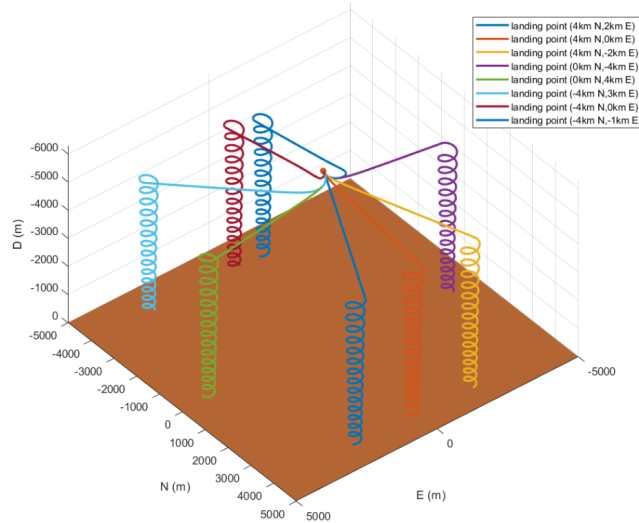


Figure 4.10: Possible landing trajectories

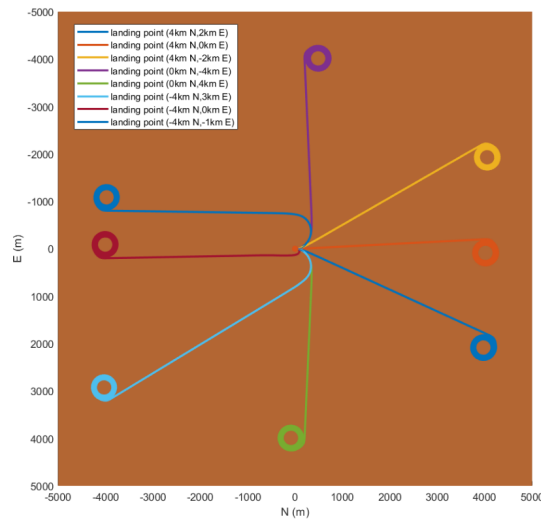


Figure 4.11: Possible landing trajectories: upper view

## 4.2 Performance with wind disturbances

So far only simulations without the presence of wind have been presented. To have a more realistic representation of the behavior of the parafoil in the martian environment, the model has been tested also with wind disturbances. Two simulations are presented, one with the wind during the approaching phase and the other with the wind during the spiral descent.

### Wind disturbance between 50 s and 450 s

The disturbance is applied in the first part of the trajectory, the linear approach. As shown in Figures 4.12 and 4.13 the parafoil shifts from the planned path due to the wind. Although its able to adjust his heading direction and reaches the landing area anyway. In Figures 4.14, 4.15 and 4.16 the variables oscillations induced by the disturbance are reported.

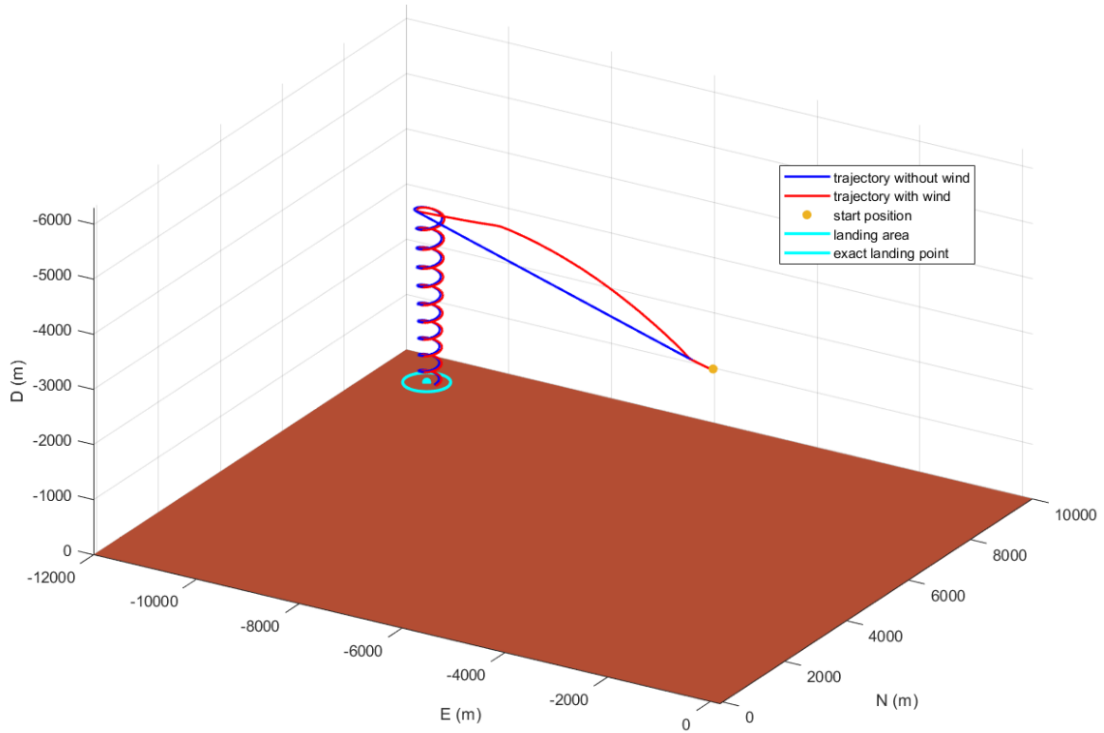


**Figure 4.12:** Comparison between trajectory with and without wind

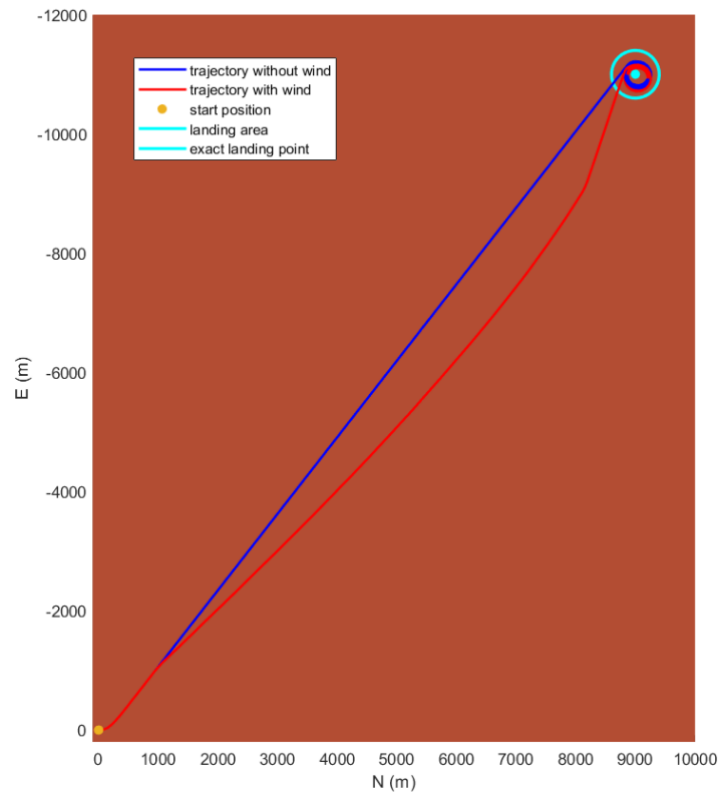


Figure 4.13: Comparison between trajectory with and without wind: upper view

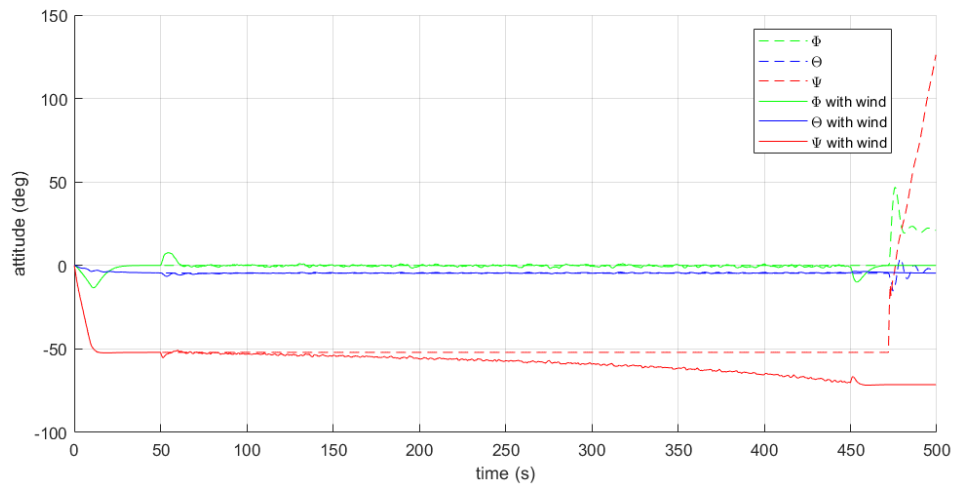
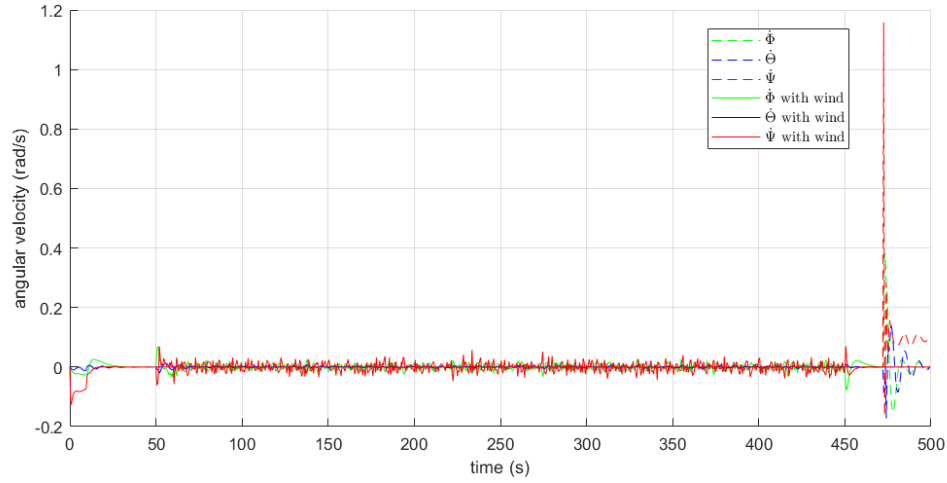
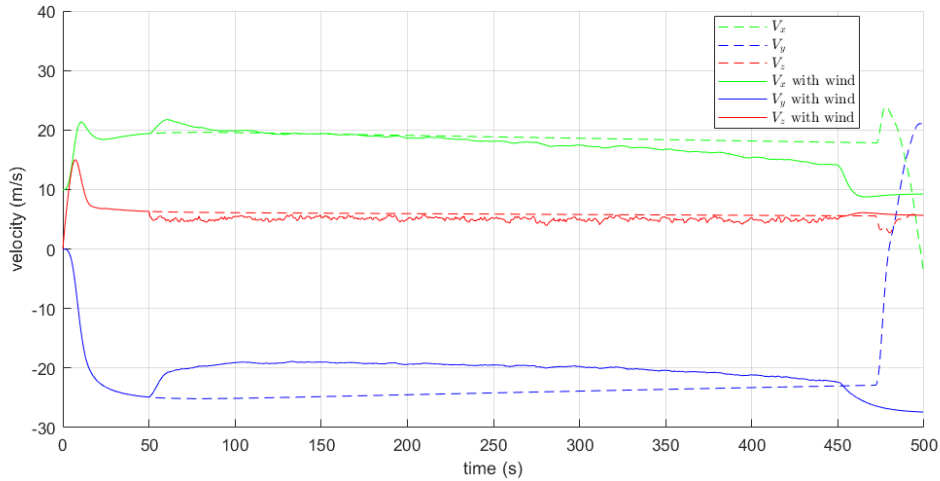


Figure 4.14: Parafoil's attitude with and without wind disturbance



**Figure 4.15:** Parafoil's angular velocities with and without wind disturbance



**Figure 4.16:** Parafoil's velocities with and without wind disturbance

### Wind disturbance between 600 s and 1000 s

In this simulation the wind disturbance is applied in the spiral descent upon the landing area. Since in this phase of the trajectory the command  $\delta_a$  is blocked, the GNC behaves like an open loop controller, thus there isn't feedback from the model. Therefore the parafoil descent in a spiral without counter the wind, which pushes the parafoil outside the landing area, as shown in Figures 4.17 and 4.18. The command saturation of  $\delta_a$  had to be reduced to  $\pm 0.5 \text{ rad}$ . Otherwise, when

the command is blocked, the parafoil roll too much due to wind, this causes an asymmetric stall of the canopy.

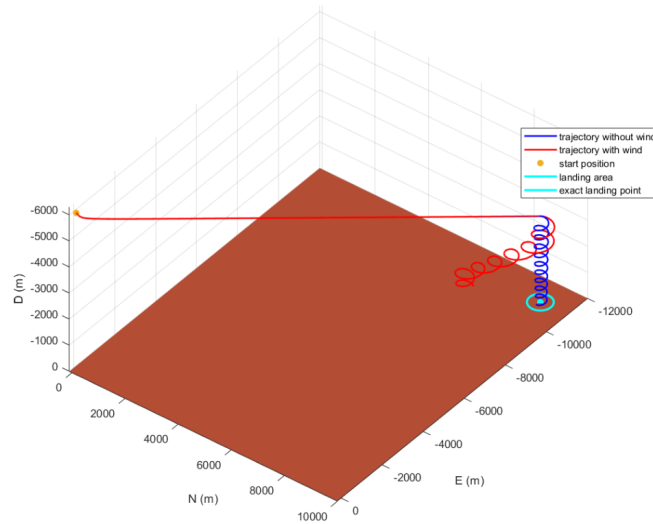


Figure 4.17: Comparison between trajectory with and without wind

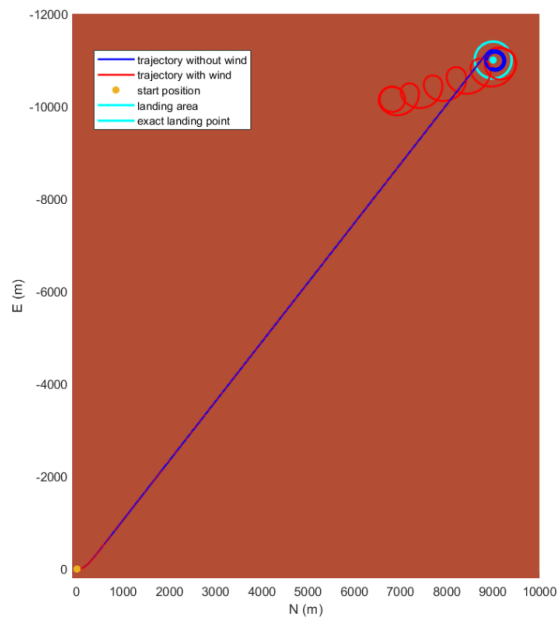
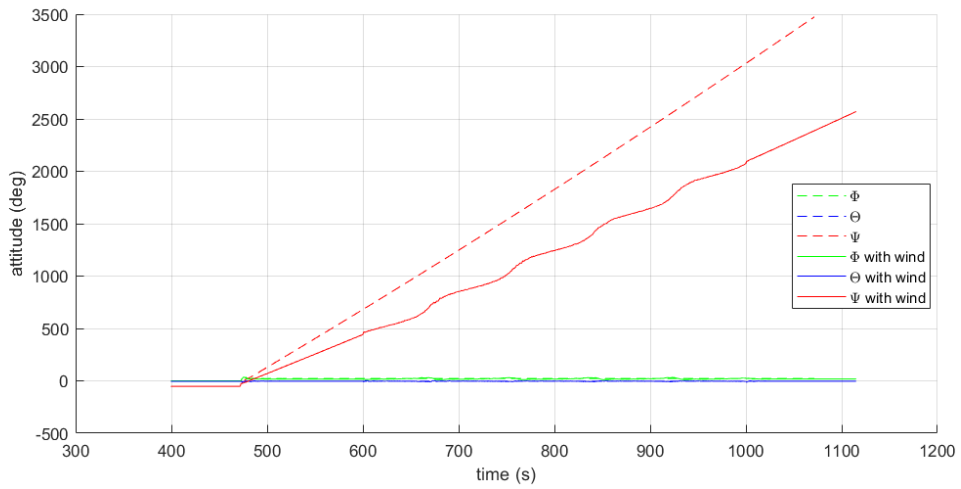
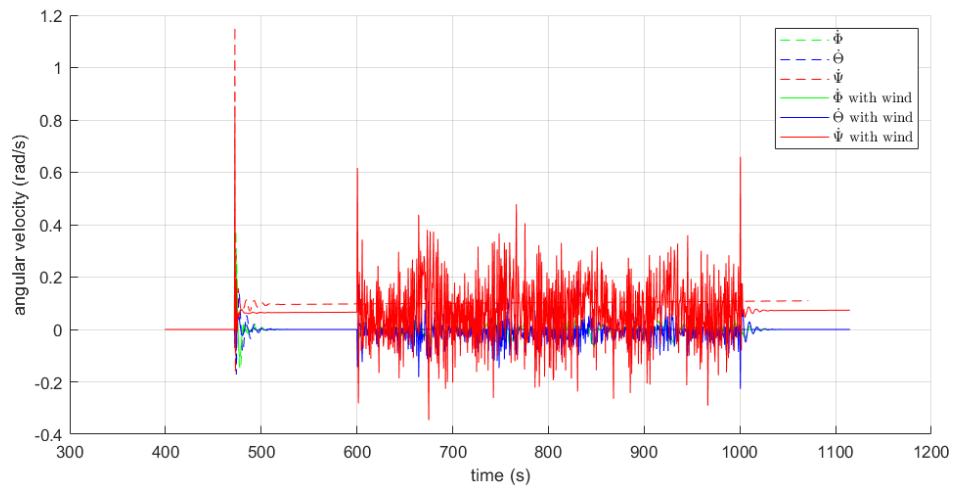


Figure 4.18: Comparison between trajectory with and without wind: upper view



**Figure 4.19:** Parafoil's attitude with and without wind disturbance in spiral descent



**Figure 4.20:** Parafoil's angular velocities with and without wind disturbance in spiral descent

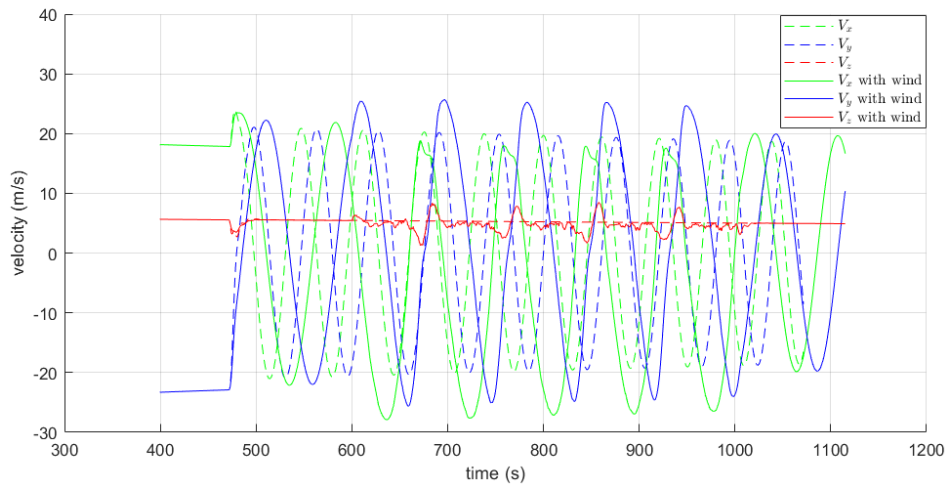


**Figure 4.21:** Parafoil's velocities with and without wind disturbance in spiral descent

To solve the problem a Simulink block has been added: when the parafoil arrives at a distance of 200 m from the landing point the command blocks and the spiral descent starts, but if the wind pushes the parafoil at a distance higher than 1000 m, the controller switches back to the closed loop control. The parafoil is so able to turn again towards the landing point and restart the spiral when the distance is lower than 200 m. The added block outputs only a value of 1 or 0. If the value is zero the closed loop control is in function, if the value is 1 the open loop control starts. In Figure 4.22 the scheme work of the block is shown, while in Figures 4.23 and 4.24 the resulting trajectory is presented.

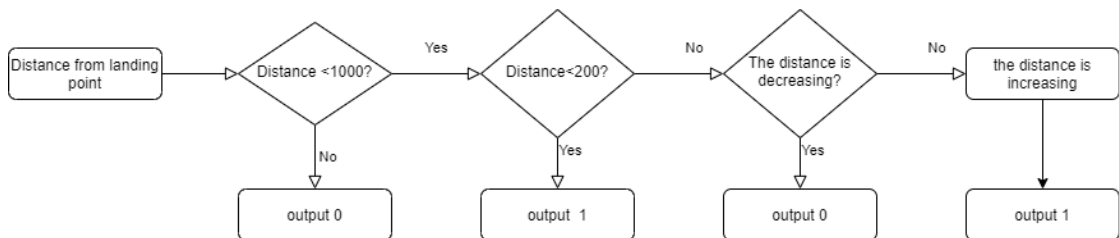


**Figure 4.22:** Switch block flow chart

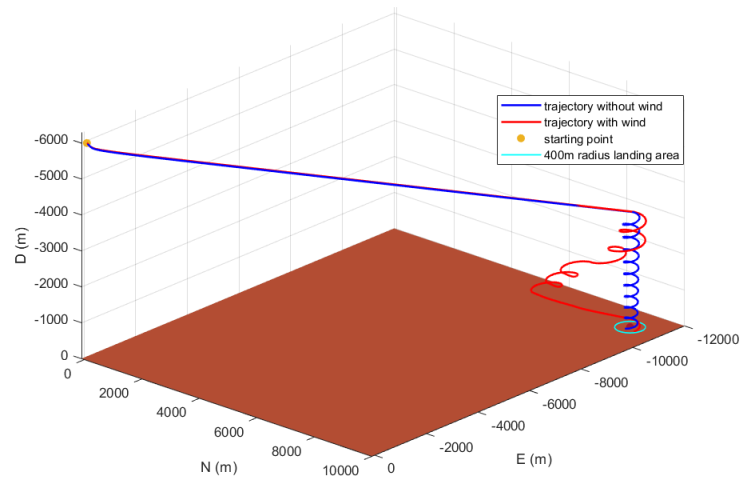


**Figure 4.23:** Comparison between trajectory with and without wind, with new switch block

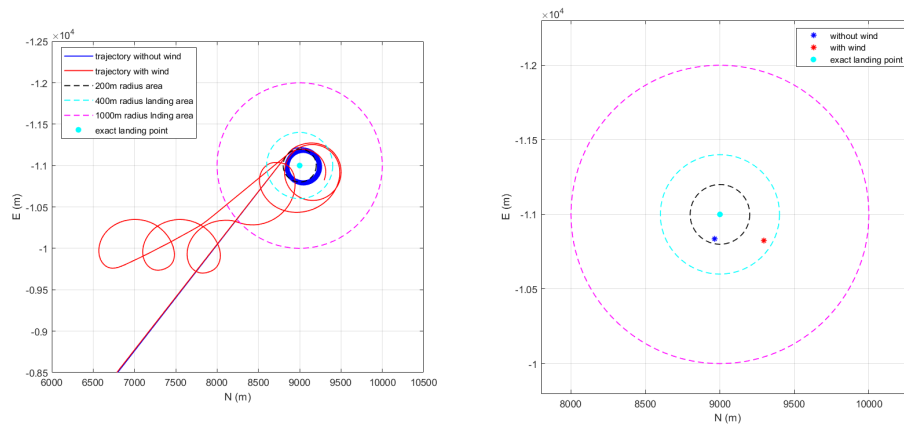


**Figure 4.24:** Comparison between trajectory with and without wind, with new switch block: upper view

# Chapter 5

## Conclusion and future works

### 5.1 Conclusion

The aim of this thesis was to study the feasibility of using two types of aerobots in the martian environment: a quadcopter drone and a parafoil system. Two very different aerial platforms with many advantages. The drone can be used to explore hazardous places in the martian landscape, while the parafoil is able to perform a precise autonomous rover landing. In this thesis the features and simplified dynamics models of both aerobots have been presented, but the focus of the work has been on the parafoil system. To study its behavior in the martian atmosphere, a 6 DoF dynamics simulator has been developed. The designed parafoil model is stable in longitudinal and lateral-directional flights. Moreover a simple trajectory composed of a linear approach towards the landing site, followed by a spiral descent upon the area, has been selected. A guidance law presented in [5] is implemented in the GNC system of the model, to control the parafoil and perform the planned route.

To improve the precision of the trajectory, instead of following the exact landing point during the approaching phase, the parafoil follows a line tangent to a circular area around the landing point, with a 200 m radius. With this type of trajectory the landing dispersion error is always lower than 400 m. Moreover, it has been shown that the simulator is able to reach almost every site around the parafoil's deployment point within 30 km. Problems occur only when the heading vector is turned of  $180^\circ$  relative to the desired direction.

To verify the robustness of the GNC system, the model has been tested with wind disturbance. The chosen control law is capable of control the parafoil's motion in presence of wind during the approaching phase, but not during the spiral descent,

due to the fact that the controller switches to an open loop control during this phase. Thus no feedback is present. The landing dispersion error increases considerably if a wind disturbance occurs during the spiral descent. To improve the precision of the landing in presence of wind, a more complex switch block has been added. The system is able of switching again to the closed loop controller, if the wind moves it at a distance higher than 1000m from the landing point. Thereby the parafoil is able to go back upon the landing area and re-start the spiral descent. With this algorithm the dispersion error, due to the wind disturbance, decreases considerably.

## 5.2 Future works

This thesis was only a preliminary study of feasibility of a parafoil system in a martian environment. Future works could improve the model and create a more accurate simulator. Here are some recommendations:

- *Choose more accurate dynamics model:* the parafoil system can be described with a 7, 8 or 9 DoF dynamics model, instead of using a 6 DoF model. These models are more accurate and take into account the rotations and oscillations of the payload relative to the parafoil. The payload and the parafoil are not considered as a single rigid body.
- *Use more accurate model of the martian atmosphere:* In this study a simplified model of the martian atmosphere has been used. In a future work a more precise atmospheric model like Mars GRAM, developed by NASA could be implemented to analyze the system performances on Mars.
- *Make an accurate aerodynamic analysis of the parafoil and the rover:* a CFD code could be used to determine in an accurate way the aerodynamic coefficients of the parafoil and the rover. Furthermore a better wing shape or airfoil could be selected for a better performance in the martian atmosphere, where the Reynolds number is lower than on Earth.
- *Select a different control law:* a more robust and complex controller could be choose for the parafoil system. Furthermore a more complex trajectory, to land exactly on the target, could be implemented. A trajectory control could be used to change the inputs at each step, re-planning the trajectory during the flight. In this way the system would be able to adjust the trajectory according to the external disturbances, or choose the best landing site after an initial reconnaissance.



# Appendix A

## Drone's dynamics simulator

The mathematical model is only one part of the simulator; it describes the evolution of the drone's motion. However, to complete the simulator it is necessary to physically characterize the drone and select an appropriate guidance and control algorithm. This chapter discusses the procedures carried out for the sizing of the drone and subsequently the implementation and tuning of the guidance and control algorithm. In fact, for the type of mission chosen, it would be unthinkable not to provide an autonomously guided aircraft. In figure A.1 is shown the final structure of the simulator which is divided into 4 main blocks:

- *Motion's Equation*: it contains the gravity, the atmosphere and the drone's model discussed respectively in the 2nd Chapter.
- *Actuators*: that has the model of the electric motors.
- *Sensors*: simulate wind disturbances presented in the 2nd Chapter, as well.
- *Guidance & Control*: contains Guidance & Control algorithms that lead the drone towards the desired target by receiving as input the vector of states read by the sensors and returning to the actuators the actions they must perform.

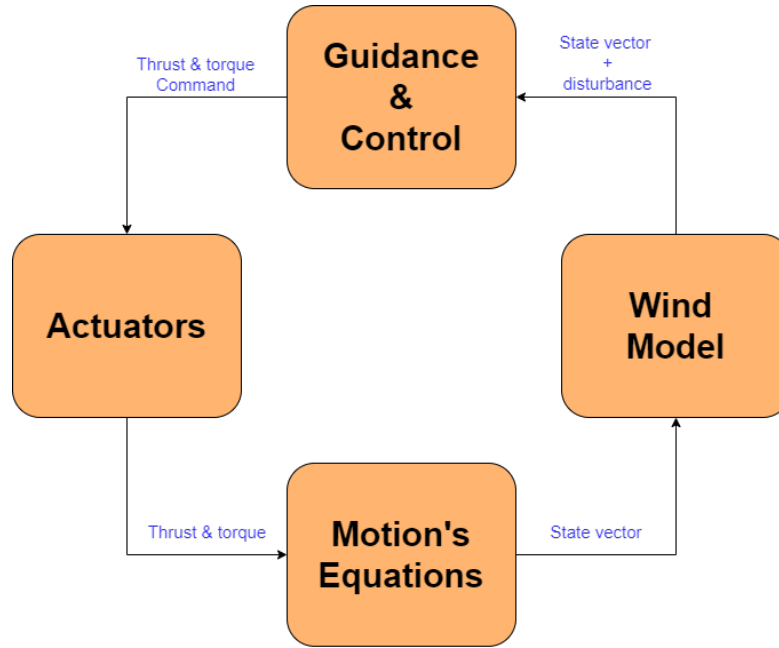


Figure A.1: Drone's simulator

## A.1 Drone configuration

Once the *Equations of Motion* has been implemented, it's necessary to define the numerical values of the constants that make up the equations. They depend on the physical structure, geometry, choice of motors and propellers and their relative coupling. Therefore choosing the number of propellers and their arrangement, as done before, is not sufficient to complete the mathematical model but are just some inputs. These parameters are closely linked, so if the input data are not sufficient to define them uniquely, iterative loops must be used.

The principal characteristics needed to define the drone configuration are here reported.

### The propellers

The aerodynamic characterisation of the propeller is an important step in determining the propulsive capabilities of the drone. This can be done using the *Blade Elementary Theory*, which predicts the value of force, torque and mechanical power required by the propellers [23]. Since this is only a preliminary study, to estimate the performances of propellers in Mars atmosphere,  $C_T$  and  $C_Q$  values have been taken from Ref. [23]. In which tests have been conducted under indoor conditions in the *TerraXcube*, a hypobaric climatic laboratory where is possible to set different

extreme environmental conditions such as humidity, solar radiation, rain and snow temperature (from  $-40^{\circ}\text{C}$  to  $40^{\circ}\text{C}$ ) and pressure (from sea level up to  $300\text{mbar}$  -  $9000\text{mbar}$ ), in order to focus on how harsh environments (low temperature and pressure) influence unmanned vehicle performance.

$C_T$  and  $C_Q$ , are defined as:

$$c_T = \frac{T}{1/2\rho D^4 n^2} \quad (\text{A.1})$$

$$c_Q = \frac{Q}{1/2\rho D^5 n^2} \quad (\text{A.2})$$

Where  $T$  is the thrust,  $Q$  is the propeller torque,  $\rho$  is the air density,  $n$  is the angular speed in rev/min and  $D$  is the diameter of the propellers.

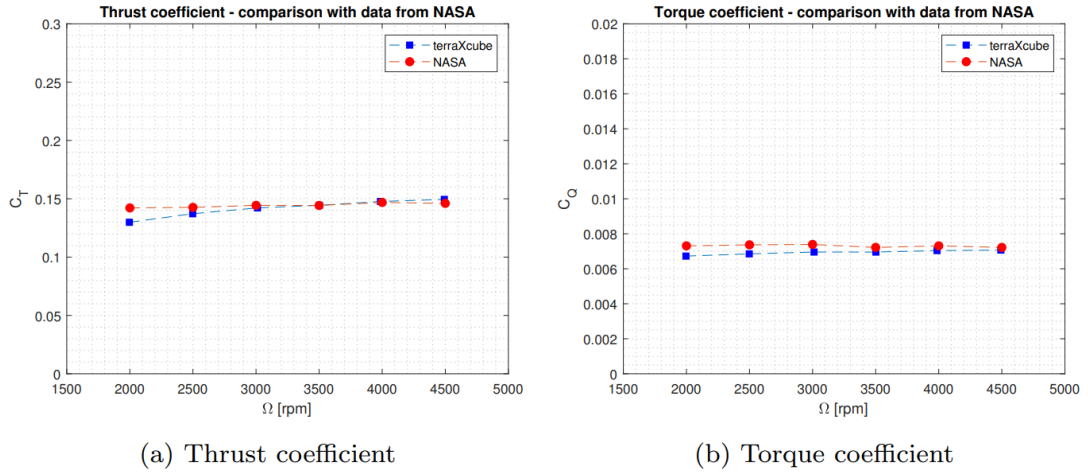


**Figure A.2:** Values of  $C_t$  and  $C_q$  as the angular velocity varies

Another fundamental step in propeller modelling is the determination of mass and geometry. To do this, data are collected for model helicopter propellers and drones. A graph showing the mass trend as a function of radius, shown in Figure A.3. The interpolation provides two different curves, one linear, the other parabolic. The parabolic curve has been used to obtain the most accurate mass estimate possible.

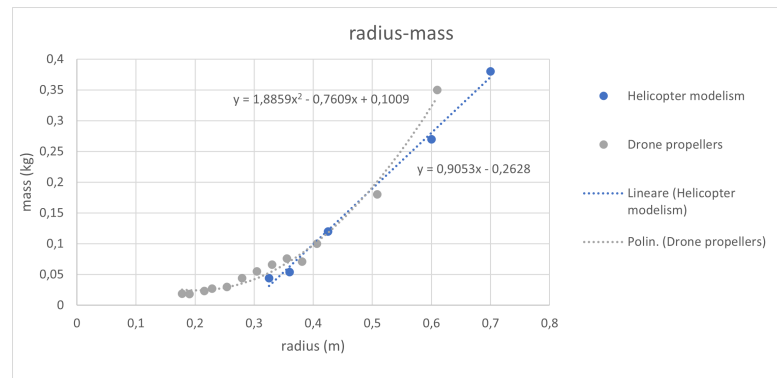


**Figure A.3:** mass as a function of radius for drone propellers and model helicopter propellers

The sizing of the physical and geometry characteristic of the drone led to the choice of a propeller with the following characteristics.

Radius	0,40 m
Mass	0.200 Kg
P max rot	6,01 W
Q max rot	0.0957 Nm
T max rot	2,24 N
omega max	3636 RPM
omega hover	2700 RPM
P max tot	24,04 W
P hover rot	2,15 W
P hover	8,6 W
P media	16,32 W

**Table A.1:** Selected propeller's data

### Electric motors and Batteries

The sizing of the propeller involves the choice of a suitable electric motor capable of satisfying the torque and angular speed requirements. Brush-less type motors are selected for this type of mission; in fact, they are the ones that best suit the Martian

atmosphere and, in general, missions where it is not possible to do maintenance, thanks to the absence of brushes that wear giving rise to dust or high heat that could compromise the operational life of the system.

The choice of the type of motor depends strongly on the power required by the propeller. Each rotor needs a mechanical power in the case of maximum angular speed equal to:

$$P_m = Q \cdot \omega_{max} \quad (\text{A.3})$$

Where  $Q$  is computed from equation A.2 and  $\omega_{max}$  is chosen from table A.1 so that the Mach at the tip does not exceed 0.7 .

The motor must be able to provide, therefore, an equal power, also considering losses and a non-unitary efficiency. In relation to this, along with an excellent power-to-weight ratio and the wide temperature range it can withstand, the DJI-E305 is selected as one of the possible motors [24].

Temperature range	from -10 to 40 °C
Max voltage	17,4 V
Max current	20 A
Max peak current (3 seconds)	30 A
ESC mass	0,027 kg
Stator mass	0,056 kg

**Table A.2:** DJI E305 peculiarity

Knowing the motors parameters it's possible to choose the batteries features, in order to satisfy the power request of the motors. For this purpose a lithium polymer battery with the characteristics described in Table A.3 has been chosen.

Temperature range	from -20 to 60 °C
Capacity (C)	1800 mAh
Discharge rate $r_c$	40 1/h
Voltage (V)	14,8 V
Current (I)	72 A
Energy density ( $\xi$ )	1133,2 Wh/kg

**Table A.3:** lithium polymer battery (Li-Po S4) peculiarity

Note how the current value is much higher than the maximum value tolerated by the single motor. It is worth remembering, however, that the same battery supplies power to the four motors of the drone, which are in parallel. Each of them receive a quarter of current, that is below the maximum tolerable limit.

### Total mass and Inertia tensor

The mass calculation involves the sum of 3 main elements:

1. **Body mass** ( $m_c$ ): Battery mass ( $m_b$ ) can be calculated from the specific energy of the battery. Once the energy has been calculated, in fact, from the following formula it is possible to obtain its weight:

$$m_b = \frac{E}{\xi} \quad (\text{A.4})$$

Where  $\xi$  is the *Battery's specific energy* expressed in  $\frac{\text{Wh}}{\text{kg}}$ , and  $E = V \cdot C$  is the total output energy of the battery.

The body is composed of the battery plus a possible payload system with thermal coatings. As a first approximation, it has been estimated that the battery constitutes 50% of the weight of the central body, therefore:

$$m_c = 2 \cdot m_b \quad (\text{A.5})$$

2. **Propeller mass** ( $m_p$ ): It is obtained once the radius of the blades is fixed, with the parabolic interpolation presented in Figure A.3.
3. **Motor mass** ( $m_m$ ): For simplicity it has been considered the mass of the motor DJI E305, reported in Table A.2.

Total mass is equal to:

$$m = m_c + 4(m_p + m_m) \quad (\text{A.6})$$

The Moment of Inertia depends from the geometry and the mass distribution. In this work a basic model is presented in which the central body is schematized by a cube of side  $l$  and the rotors with their motors by 4 flat discs with uniformly distributed mass, each one has a diameter equal to the rotor's diameter. Thus, 2 main contributions to total inertia should be calculated:

- **Rotor's inertia:**

$$\begin{aligned}
 Jx_r &= \frac{1}{4} \cdot m_{rotor} \cdot r^2 \\
 Jy_r &= Jx_r \\
 Jz_r &= \frac{1}{2} \cdot m_{rotor} \cdot r^2
 \end{aligned}
 \tag{A.7}$$

- **Body inertia:**

$$\begin{aligned}
 Jx_c &= \frac{1}{6} \cdot m_c \cdot (l)^2 \\
 Jy_c &= Jx_c \\
 Jz_c &= Jx_c
 \end{aligned}
 \tag{A.8}$$

Obviously, the contribution of the rotors must be multiplied by 4 and cannot simply be added to the inertia of the body: the transport moment must be considered. In order to do this, it has been assumed that the drone is perfectly symmetrical and the mass distribution is uniform. So the **Total inertia** is equal to:

$$\begin{aligned}
 Jxx &= 4 \cdot (m_{rotor} \cdot (L^2 + h^2) + Jx_r) + Jx_c \\
 Jyy &= 4 \cdot (m_{rotor} \cdot (L^2 + h^2) + Jy_r) + Jy_c \\
 Jzz &= 4 \cdot (m_{rotor} \cdot 2L^2 + Jz_r) + Jz_c
 \end{aligned}
 \tag{A.9}$$

$$J = \begin{bmatrix} J_{xx} & 0 & 0 \\ 0 & J_{yy} & 0 \\ 0 & 0 & J_{zz} \end{bmatrix}
 \tag{A.10}$$

Where  $L$  is the distance between two adjacent rotors and  $h$  is the distance between the rotor's CoM and central body's CoM.

### A.1.1 Iterative loop

As said before, the elements presented so far are dependent on each other. An iterative loop is used to define them completely.

First, a hypothetical mass that the drone could have as a whole is selected. The thrust is calculated so that it is twice the weight force of the drone:

$$T = \frac{mg \cdot K_{T/W}}{n_{rot}}
 \tag{A.11}$$

Where  $n_{rot}$  is the number of rotors and  $K_{T/W} = 2$  is the *Thrust to Weight ratio*. Using the formulations described above, with the iterative loops the following

drone's characteristics have been defined. In Figure A.4 the work scheme of the iterative loop is shown. Moreover in Table A.4 the results of the algorithm are reported.

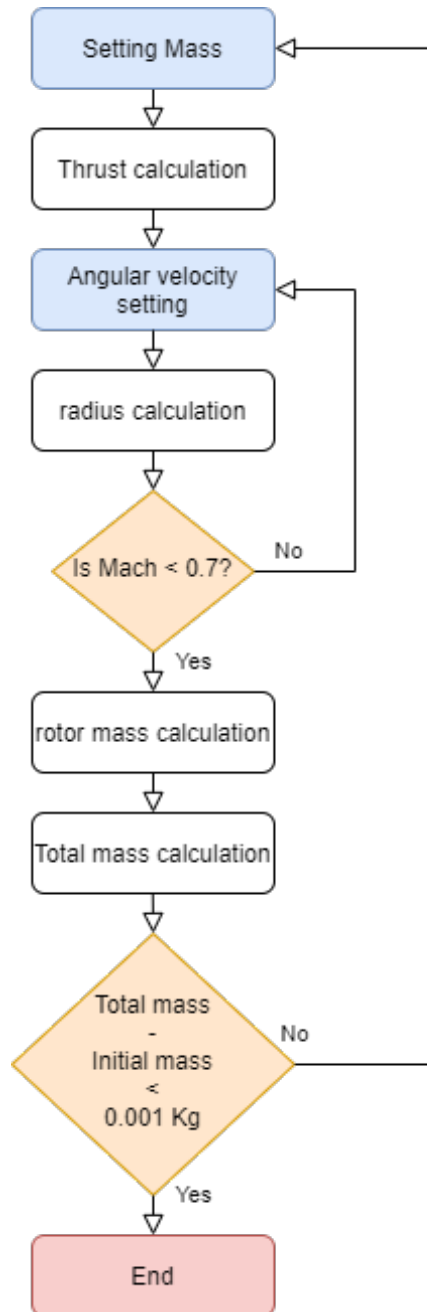


Figure A.4: Drone's flowchart

Drone configuration parameters	
Mass	1.28 kg
arm length	0.72 m
Max angular velocity	3636 RPM
$J_{xx}$	0,2514 $\text{kgm}^2$
$J_{yy}$	0,2514 $\text{kgm}^2$
$J_{zz}$	0,4961 $\text{kgm}^2$

Table A.4: Drone configuration parameters

## A.2 Guidance and Control

In order for a feasibility analysis to be conducted, the system must be able to perform certain maneuvers. It means to indicate to the drone a destination to reach through an appropriate guidance; at the same time, it must be ensured that it actually reaches these points. The controller performs this role by analyzing the states (position velocity attitude and angular velocity) in such a way that the assigned target is reached while maintaining stability and avoiding behaviors that would compromise the success.

In the next sections the models of the guide and the controller are presented.

### A.2.1 Guidance algorithm

Creating a guidance algorithm is a very complex task, in the case of this mission it is wanted that the drone reaches specific points. Linking them together we obtain a trajectory. Following this idea it has been decided to realize a point tracker.

First, the desired position  $x_{des}$  is compared with the current position  $x_{act}$ , that comes from the sensors and can therefore be affected by errors, which, in this case, have been modeled as arising solely from the wind. The difference between these two factors is the input signal to generate a square wave: if it is less than a certain threshold (i.e. how precisely the desired position is to be reached) the output signal is equal to 1, vice versa it is equal to 0. A counter increments a index only if it detects a *rising edge* condition. All desired positions are contained within an array, which has a point in each row and the counter indicates which row of the matrix should be read. The new vector containing the 3 coordinates of the new desired position is given to the controller.

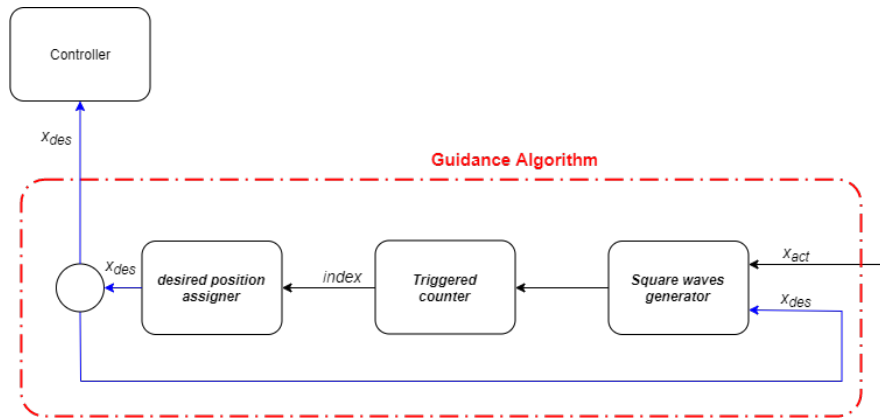


Figure A.5: Guidance algorithm structure

### A.2.2 Control design

The type of control chosen to test the drone is the PID, it develops the command based on the error and its trend; in fact it applies three operations to the error that are then overlapped:

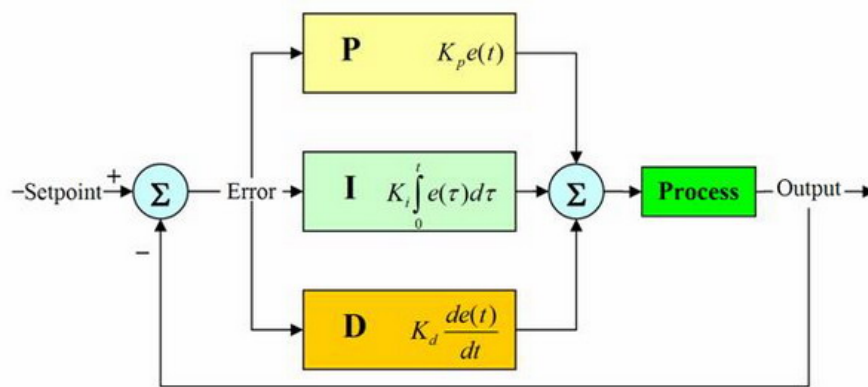


Figure A.6: PID controller basic structure

- *Proportional* that provides a command proportional ( $k_p$ ) to the error, it allows to quickly bring the system to the values of regime, however it renders the system unstable causing oscillations in the around of the desired one;
- *Integrative* that integrates the error using an accumulator, which is then multiplied by an appropriate gain, this type of operation allows to correct the error at steady state, but as the proportional controller makes the system

unstable;

$$\eta(t) = k_i \int_0^t e(t)dt \quad \text{or} \quad \eta(s) = \frac{k_i}{s}e(s) \quad (\text{A.12})$$

- *Derivative* that consists in applying an anticipatory filter able to correct steady-state instabilities, this is the main advantage of the latter component of the PID, however, this comes at a cost in terms of steady-state reach time, *rising time*, which could become excessively long. In addition, this type of filter is particularly subject to errors, since it depends on the derivative of the error. For this reason also in this case it is advisable to set a suitable gain multiplier or adopting particular solution as described below.

$$\eta(t) = k_d \frac{de}{dt} \quad \text{or} \quad \eta(s) = k_d s e(s) \quad (\text{A.13})$$

Adding up all three effects it is possible to reduce the disturbances of the single ones obtaining a quite effective controller [22].

$$u(t) = k_p e(t) + k_i \int_0^t e(t)dt + k_d \frac{de(t)}{dt} \quad (\text{A.14})$$

There are four variables to be controlled (position, velocity, attitude and angular velocity) so four controllers are required. The motion of the drone, however, makes them interdependent making often necessary a cascade architecture: within it each PID controls a variable and the error that it receives is nothing more than the output of a previous one, except for the top that has as input directly the position error.

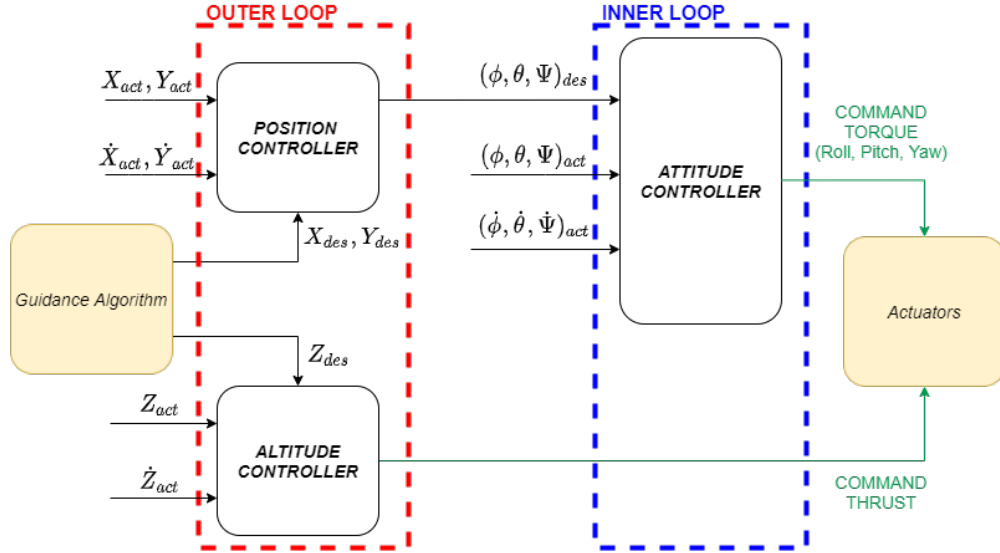


Figure A.7: Cascade controller structure

Position and velocity controllers are located in the outer loop, while attitude and angular velocity in the inner loop. This architecture has several advantages, like the possibility of linking the attitude to the translation of the drone so as not to have undesired behaviors.

### A.3 Actuators

The components of the command enter inside the actuation, this provides that the command signals are transformed into voltage by a special *Motor Mixer*. The voltage, within the motor's electrical circuit, provides a current that sets the propellers in motion. Therefore, the current is proportional to the voltage, which in turn depends on the command. What actually happens to the system is a dual delay due to the electronics of the *Motor Mixer* and the actuation time of the mechanical part of the motors due to its inertia. Modeling the *Motor Mixer*, however, is a choice that leads to the subsequent development of hardware and therefore could be costly. In the present work, it is not modeled, but these delays were added via special functions to account for them.

### A.4 Test and Results

Once the flight simulator has been developed, in order to complete the feasibility analysis, several maneuvers must be carried out to allow conclusions to be drawn regarding the reliability of the guidance and, above all, the control adopted. For each of them, the states are analysed and factors such as the accuracy in reaching a specific waypoint, the ability to reach certain speeds, the stability of the attitude and thus also the resulting oscillations are discussed. Tests are conducted both in the presence and absence of wind in order to evaluate the response to a typical disturbance on Mars. In fact, the wind disturbs the sensors when detecting speed, providing the controller with an error-affected measurement that, due to its architecture, inevitably leads to a drop in performance. To highlight these effects, different maneuvers are discussed in the following paragraphs; specifically, the first maneuver is used to understand how the drone responds to the request to maintain a specific point in space, while the other is composed of a series of waypoints. The main difference is that in the latter case, for each point reached, errors accumulate due to inaccuracy, and between one waypoint and another the conditions are not perfectly stationary, so it's possible to see how the system reacts once the next target has been acquired.

### A.4.1 Hovering

Hovering is a particular type of flight that occurs when the drone is stationary in the air at zero speed and constant altitude. In this case, one speaks of stationary flight or point flight, as the drone's course in space indicates a simple point. The hovering function is ideal for taking photos that are not blurred. In the generic case let's assume that the drone is at a height of 10 metres with  $\theta = 0$  and  $\psi = 0$  and let's run the simulation for a certain time interval. In the absence of wind, the drone maintains its position perfectly without oscillating. The starting position is  $pos = [0, 0, -10]$  and the desired one is the same, while all the initial velocities are null. Note that the negative value along the D axis is due to the reference system and indicates how high the drone is above the ground. During this condition all the four propellers turn at the same speed and produce the same thrust. Note that initially the drone loses a few centimetres of altitude, this problem is related to the fact that the simulator does not have initial conditions regarding the rotation speed of the propellers or the thrust. For a few steps of integration the system falls under the effect of gravity, until the controller activates the thrust command. This defect is of a simulative nature and not attributable to the dynamic behaviour of the drone. To avoid this defect, subsequent simulations are carried out by always taking off from the ground.

As can be seen from the graphs A.8 after an initial transient the final position taken is quite different. This is a sign that the controller is unable to settle at the exact desired point. It is observed that the drone oscillates along the Down direction by about 5 cm, while the biggest error is in the North direction, which is also the axis where the wind intensity is greatest. Obviously this is not by accident, the current in fact interferes with the sensors that provide the controller with different speeds with respect to the NED system and the difference between the two values is proportional to the amplitude of the disturbance.

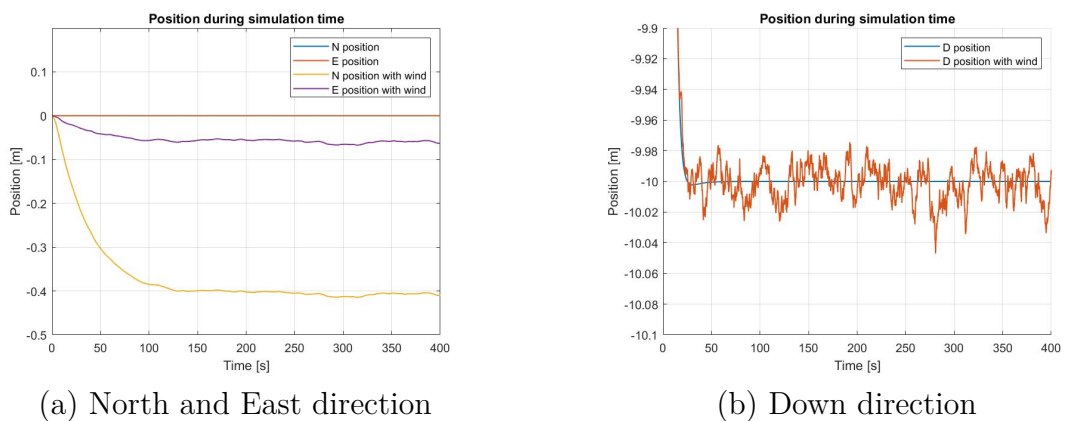


**Figure A.8:** Error in caused by wind during Hovering maneuver

What happens in the initial instants is that the drone is actually stationary with respect to the ground so the position control returns a desired speed of zero, however the sensors register a movement of the system caused by the wind. The difference between these two signals then generates a command that causes an error. As expected, the control is in fact oscillatory and fails to dampen its effect even with the passing of time, which also has an impact on the attitude. The greatest effect, as can be seen, is felt in the yaw angle, which oscillates around values of eight degrees during gusts, whereas in the nominal condition it should be zero. This is due to the controller's calculation of the desired yaw angle. It depends on the ratio of position errors in the N-E plane. The values are compared and as a result, errors of this type can be generated.

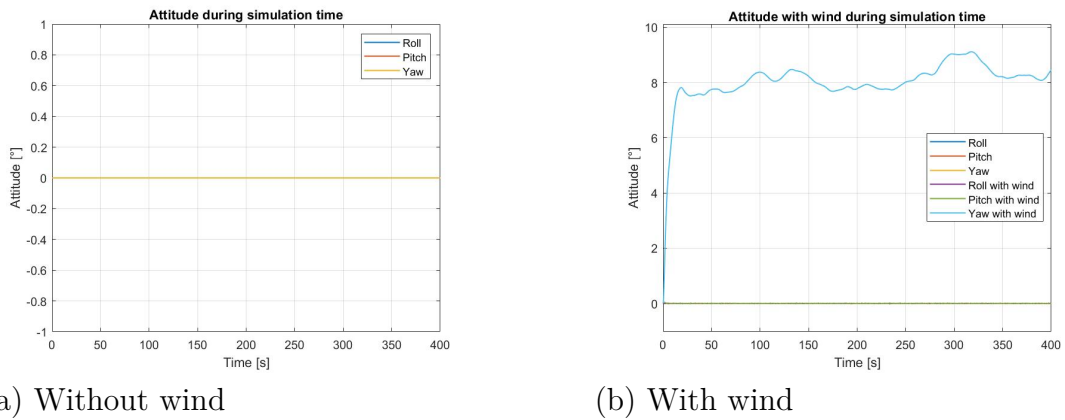


**Figure A.9:** Attitude angles during Hovering maneuver

## A.5 Square maneuver

The last maneuver involves reaching several waypoints. The aim is to demonstrate that the position error remains constant despite the accumulation of several desired positions thanks to the appropriate saturations provided in the controller. Starting from zero altitude, the drone reaches a fixed height and reaches the four vertices of a square, describing an area of approximately  $400 \text{ m}^2$ .

The system behaves as if it were carrying out a series of simple translations, following all the peculiarities discussed in the previous paragraph. However, it should be pointed out that in windy conditions a lower degree of manoeuvring precision must be required of the system. If this were not the case, the aerobot would try in vain to reach a given waypoint, ignoring the presence of the current, thus the counter wouldn't increment and the next waypoint wouldn't be read because the minimum proximity condition isn't satisfied.

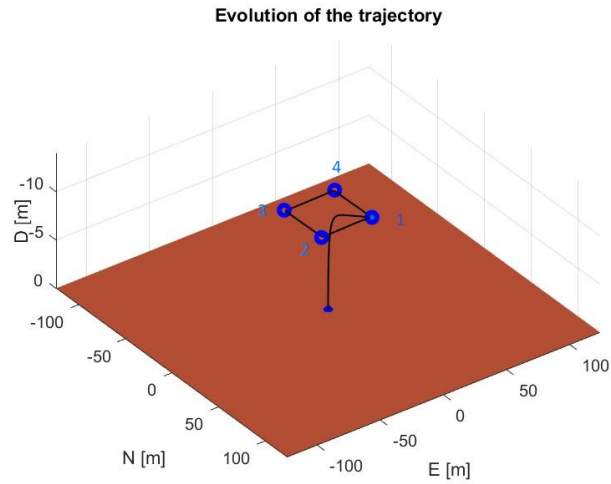


Figure A.10: Trajectory of the drone in Square maneuver

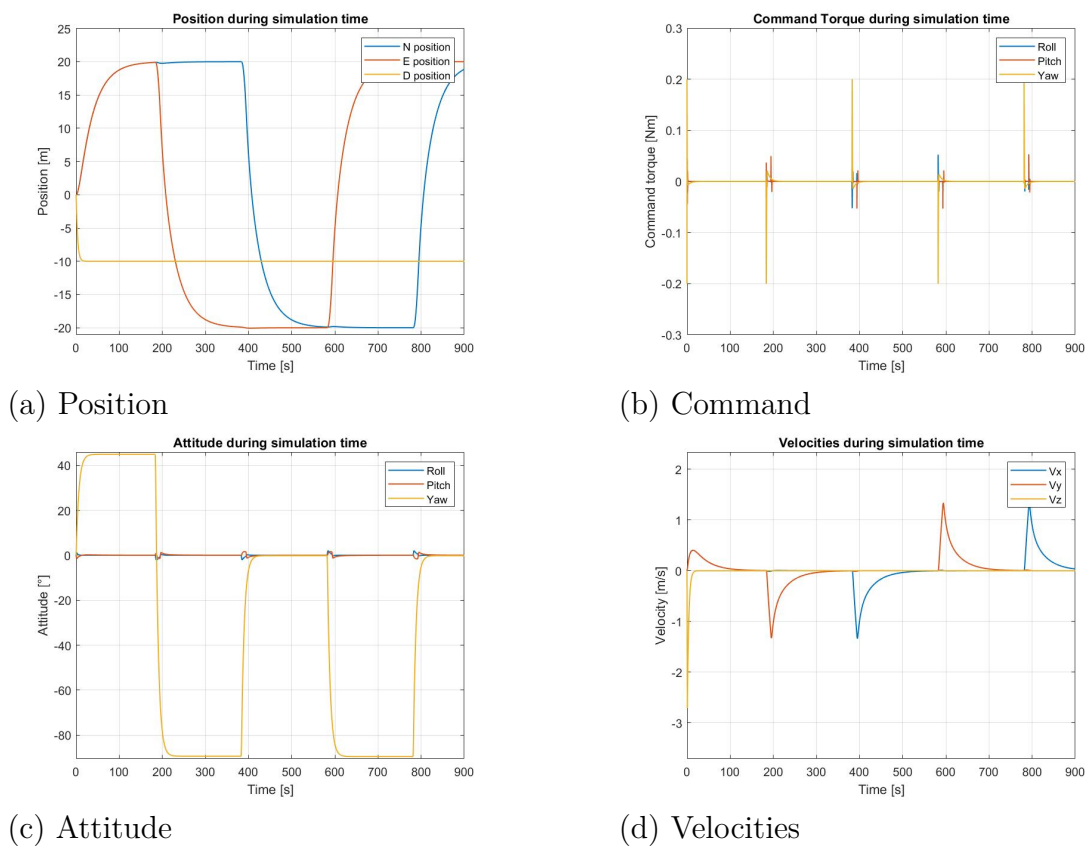


Figure A.11: Output of Square pattern

## A.6 Conclusions

The aim is to carry out a feasibility study on the possibility of a flight on Mars and his maneuvering capabilities. It has therefore been equipped with a guidance algorithm and a special controller to perform the maneuvers. In particular, a cascade architecture formed by a sequence of PID controllers has been chosen. By carrying out simulations in Matlab/Simulink, different configurations can be tested by tuning the controller parameters. With the values found, trajectories are obtained that are fairly faithful to the desired ones. However, by adding windy conditions, all the limits of the PID are shown. In particular, the errors in position with respect to the previous condition increase and the instability continues at the same rate. Nevertheless, these position errors are acceptable for the tasks that a drone is generally required to perform. However, in the case where the drone is used as an image or data acquisition device, so it is assumed to have a payload, more stringent attitude requirements are inevitable. In this case, the PID cannot meet these requirements and is not robust enough to fulfill such tasks. In particular, the sudden change of state values, combined with wind disturbance, does not allow the controller to achieve a fluctuation-free condition.

The work therefore has several open points that can lead to a considerable improvement in results:

- **Implementing others controllers** is certainly one of the key points for future work. The choice could be for a Sliding mode controller to ensure higher stability, in this way the system would be able to acquire data by eliminating noise due to oscillations.
- **More accurate disturbance models** would allow finer parameter tuning. The main noise, in fact, is the modelled wind. However, the wind oscillates around predefined values on each axis and stays in a certain circle; because of this, it always blows stronger in one direction. This is obviously a limitation of the model.
- **Model the actuators** by entering the equations governing the operation of the ESC and the mechanical actuation part of the motors. These constitute two disturbances, the first related to the delay time of the Omhico-inductive circuits, the second related to the inertia of the motor. They delay and slightly alternate the command. Including a model of this type would also make it possible to assess the effects of varying the angular speed of the propellers on the system.

- The value of the **thrust coefficients should be calculated experimentally**, but has been found in other laboratory studies, assuming that similar components are used.
- **Implementing an Extend Kalman Filter** would improve controller performance by reducing noise from sensors
- **Try different guidance algorithms**, the current one requires reaching certain waypoints but has no requirement on arrival time. This is a key parameter for this type of mission as flight times can be reduced due to the size of the drone. It is therefore necessary to foresee that the drone can perform all maneuvers and land safely.

# Bibliography

- [1] Mostafa Hassanalian, Devyn Rice, and Abdessattar Abdelkefi. «Evolution of space drones for planetary exploration: A review». In: *Progress in Aerospace Sciences* 97 (Feb. 2018), pp. 61–105. DOI: 10.1016/j.paerosci.2018.01.003 (cit. on pp. 1, 3–8, 10–12).
- [2] Giorgio Guglieri Giovan Battista Errante and Ivano Musso. «A Methodology for the Design of a Guided Parafoil Recovery System». In: () (cit. on pp. 2, 26, 27, 29, 51).
- [3] M. B. Quadrelli, A. Schutte, J. Rimani, and L. Ermolli. «Aero Maneuvering Dynamics and Control for Precision Landing on Titan». In: *2019 IEEE Aerospace Conference*. 2019, pp. 1–16. DOI: 10.1109/AERO.2019.8742230 (cit. on pp. 2, 4, 11).
- [4] *Nasa. Mars Climate Database*. [http://www-mars.lmd.jussieu.fr/mcd\\_python/](http://www-mars.lmd.jussieu.fr/mcd_python/) (cit. on pp. 2, 19, 20).
- [5] Damian Toohey. «Development of a small parafoil vehicle for precision delivery». MA thesis. The address of the publisher: Massachusetts Institute of Technology, Mar. 2006 (cit. on pp. 2, 31, 36, 43–45, 50, 51, 67).
- [6] NASA. *Mars Fact Sheet*. 2020. URL: <https://nssdc.gsfc.nasa.gov/planetary/factsheet/marsfact.html> (visited on 03/04/2021) (cit. on p. 6).
- [7] Robert Braun, Henry Wright, Mark Croom, J. Levine, and David Spencer. «Design of the ARES Mars Airplane and Mission Architecture». In: *Journal of Spacecraft and Rockets* 43 (Sept. 2006), pp. 1026–1034. DOI: 10.2514/1.17956 (cit. on p. 8).
- [8] L. A. Young, E. Aiken, P. Lee, and G. Briggs. «Mars rotorcraft: possibilities, limitations, and implications for human/robotic exploration». In: *2005 IEEE Aerospace Conference*. 2005, pp. 300–318. DOI: 10.1109/AERO.2005.1559324 (cit. on pp. 9, 10).

- 
- [9] NASA. *Mars Helicopter Ingenuity Fact Sheet*. URL: <https://mars.nasa.gov/resources/24887/mars-helicopter-ingenuity-fact-sheet/> (visited on 03/05/2021) (cit. on pp. 9, 10).
- [10] Nathan Scott Collins. *System Design and Nonlinear State-Dependent Riccati Equation Control of an Autonomous Y-4 Tilt-Rotor Aerobot for Martian Exploration*. University of Surrey (United Kingdom), 2016 (cit. on pp. 13–16).
- [11] Hanbing Song. *A Hybrid Martian VTOL UAV: Design, Dynamics and Control*. University of Surrey (United Kingdom), 2008 (cit. on p. 14).
- [12] Wei Shyy, Yongsheng Lian, Jian Tang, Dragos Viieru, and Hao Liu. *Aerodynamics of low Reynolds number flyers*. Vol. 22. Cambridge University Press Cambridge, 2007 (cit. on p. 15).
- [13] Christian Hirt, SJ Claessens, Michael Kuhn, and WE Featherstone. «Kilometer-resolution gravity field of Mars: MGM2011». In: *Planetary and Space Science* 67.1 (2012), pp. 147–154 (cit. on p. 18).
- [14] *Nasa. Mars Atmosphere Model*. <https://www.grc.nasa.gov/www/k-12/airplane/atmosmrm.html> (cit. on p. 19).
- [15] Kanaiya Agrawal and Punit Shrivastav. «Multi-rotors: A revolution in unmanned aerial vehicle». In: *International Journal of Science and Research* 4.11 (2015), pp. 1800–1804 (cit. on pp. 22, 23).
- [16] Brian L Stevens, Frank L Lewis, and Eric N Johnson. *Aircraft control and simulation: dynamics, controls design, and autonomous systems*. John Wiley & Sons, 2015 (cit. on p. 25).
- [17] J. Lingard. «Ram-Air Parachute Design». In: *Proceedings of Precis. Aer. Deliv. Semin. (13th AIAA Aerodynamic Decelerator Systems Technology Conference)* (May 1995), pp. 1–51 (cit. on pp. 26, 36–43).
- [18] P. Lissaman and Glen Brown. «Apparent mass effects on parafoil dynamics». In: *Aerospace Design Conference*. DOI: 10.2514/6.1993-1236 (cit. on pp. 32, 33).
- [19] *JPL's Open Source build-it-Yourself Rover*. <https://opensourcerover.jpl.nasa.gov/> (cit. on p. 36).
- [20] Thomas Jann. «Aerodynamic Coefficients for a Parafoil Wing with Arc Anhedral - Theoretical and Experimental Results». In: *17th AIAA Aerodynamic Decelerator Systems Technology Conference and Seminar*. DOI: 10.2514/6.2003-2106 (cit. on pp. 38, 43).
- [21] Jasmine Rimani. «High-Lift Systems for Planetary Descent and Landing». MA thesis. The address of the publisher: Politecnico of Torino, Oct. 2018 (cit. on p. 47).

## BIBLIOGRAPHY

---

- [22] R. C. Nelson. *Flight stability and automatic control*. Boston, Mass: WCB/McGraw Hill, 1998 (cit. on pp. 50, 80).
- [23] Matteo Scanavino, Arrigo Avi, Andrea Vilardi, and Giorgio Guglieri. «UAS testing in low pressure and temperature conditions». In: *2020 International Conference on Unmanned Aircraft Systems (ICUAS)*. IEEE. 2020, pp. 1757–1765 (cit. on p. 71).
- [24] *DJI E305 motor*.  
<https://www.dji.com/it/e305/download> (cit. on p. 74).